REPORT DOCUMENTATION PAGE

Form Approved
OMB NO. 0704-0188

1. AGENCY USE ONLY (Leave Blank)	2. REPORT DATE November 1999	3. REPORT TYPE AND DATES COVERED Final Report

4. TITLE AND SUBTITLE
A Comparative Theoreticala Study of Quasi-Static and Impact Response of Laminated and Textile Composite Structures

5. FUNDING NUMBERS
DAAH04-96-1-0057

6. AUTHOR(S)
Christopher M. Pastore

7. PERFORMING ORGANIZATION NAME(S) AND ADDRESS(ES)
Philadelpia College of Textiles and Science
Philadelphia, PA 19144

8. PERFORMING ORGANIZATION REPORT NUMBER

9. SPONSORING / MONITORING AGENCY NAME(S) AND ADDRESS(ES)
U. S. Army Research Office
P.O. Box 12211
Research Triangle Park, NC 27709-2211

10. SPONSORING / MONITORING AGENCY REPORT NUMBER
ARO 35661.1-EG

11. SUPPLEMENTARY NOTES
The views, opinions and/or findings contained in this report are those of the author(s) and should not be construed as an official Department of the Army position, policy or decision, unless so designated by other documentation.

12 a. DISTRIBUTION / AVAILABILITY STATEMENT
Approved for public release; distribution unlimited.

12 b. DISTRIBUTION CODE

13. ABSTRACT (Maximum 200 words)

The report presents the details of the computational algorithm for a novel three-dimensional variational dynamic analysis approach developed in computational algorithm of impact contact problem based on variational mosaic model and numerical examples. The analysis approach is aimed at solving a variety of stress analysis problems of composite structural parts under the effect of impulsive and impact loads. Some specific applications of the developed analysis are shown on the examples of transverse dynamic bending of simply supported laminated plate and 3D contact analysis for a multi-brick structure under longitudinal and transverse longitudinal rigid body impact.

Numerical results clearly show dynamic effects in response of simply supported laminated plate at high rate of transverse dynamic bending. As the rate of transverse dynamic bending decreases the response of simply supported laminated plate reduces to the corresponding benchmark static solution tensile response of 3D woven fabrics. This example shows the capability of the developed computer code to solve 3D dynamic problems for a wide range of dynamic loading rate.

(continued on next page)

14. SUBJECT TERMS			15. NUMBER OF PAGES 16. PRICE CODE
17. SECURITY CLASSIFICATION OR REPORT UNCLASSIFIED	18. SECURITY CLASSIFICATION ON THIS PAGE UNCLASSIFIED	19. SECURITY CLASSIFICATION OF ABSTRACT UNCLASSIFIED	20. LIMITATION OF ABSTRACT UL

NSN 7540-01-280-5500

Standard Form 298 (Rev.2-89)
Prescribed by ANSI Std. 239-18
298-102

REPORT DOCUMENTATION PAGE (SF298)
(Continuation Sheet)

Numerical results for the 3D impact contact problem illustrate time variations of the target displacements, strains and stresses as well as the time variations of the projectile displacement and velocity and impact contact pressure obtaied from solution of the coupled problem for mechanical system "projectile-target".

Considered numerical examples validate applicability and verify accuracy of the developed computational algorithm and computer code.

FINAL REPORT

A Comparative Theoretical Study of Quasi-Static and Impact Response of Laminated and Textile Composite Structures

Army Research Office Grant DAAH04-96-1-0057

Christopher M. Pastore

School of Textiles and Materials Technology

PHILADELPHIA
UNIVERSITY

Alexander E. Bogdanovich

3Tex, Inc.

1999

TABLE OF CONTENTS

0. SUMMARY

The report presents the details of the computational algorithm for a novel three-dimensional variational dynamic analysis approach developed in [1, 2]. The analysis approach is aimed at solving a variety of stress analysis problems of composite structural parts under the effect of impulsive and impacts loads. Some specific applications of the developed analysis are shown on the examples of transverse dynamic bending of simply supported laminated plate and 3D contact analysis for a multi-brick structure under longitudinal and transverse longitudinal rigid body impact.

Numerical results clearly show dynamic effects in response of simply supported laminated plate at high rate of transverse dynamic bending. As the rate of transverse dynamic bending decreases the response of simply supported laminated plate reduces to the corresponding benchmark static solution [3]. This example shows the capability of the developed computer code to solve 3D dynamic problems for a wide range of dynamic loading rate.

Numerical results for the 3D impact contact problem illustrate time variations of the target displacements, strains and stresses as well as the time variations of the projectile displacement and velocity and impact contact pressure obtained from solution of the coupled problem for mechanical system "projectile-target".

Considered numerical examples validate applicability and verify accuracy of the developed computational algorithm and computer code.

1. COMPUTATIONAL ALGORITHM OF IMPACT CONTACT PROBLEM BASED ON VARIATIONAL MOSAIC MODEL

The methodology of impact contact interaction modeling based on the variational Mosaic Model has been described in Chapter 2 of the 1998 Interim Report [2]. Relations (2.24), (2.25) and (2.30) of [2] describe governing equations of the impact contact problem. The details of the algorithm for numerical solution of these governing equations are given below.

1.1. LAGRANGIAN FUNCTION OF DYNAMIC IMPACT CONTACT PROBLEM

The three-dimensional variational analysis approach presented here for mechanical system "mosaic composite body-rigid projectile" is based on Hamilton's variational principle

$$\delta \int_{t_1}^{t_2} \mathbf{L}(t)\, dt = 0 \tag{1.1}$$

where $\mathbf{L}(t)$ is the Lagrangian function written for the interacting composite target and rigid projectile. This function is defined as following

$$\mathbf{L}(t) = K_p(t) + \sum_{s=1}^{S} \left[K^{(s)}(t) - P^{(s)}(t) + W^{(s)}(t) \right] + V_{PT}(t) \tag{1.2}$$

where

$$K_p(t) = \frac{1}{2} M_p \left(\dot{U}_p(t) \right)^2 \tag{1.3}$$

is the kinetic energy of the projectile, $\dot{U}_p(t) = \frac{dU_p(t)}{dt}$, M_p is the projectile mass, and U_p is the unknown projectile velocity;

$$K^{(s)}(t) = \frac{1}{2} M_p \left(\dot{U}_p(t) \right)^2 \tag{1.3}$$

is the kinetic energy of the s^{th} brick, $\dot{U}^{(s)}(t) = \frac{dU^{(s)}(t)}{dt}$, and $U^{(s)}(t)$ is the vector of the undetermined displacement approximation coefficients of the s^{th} brick;

$$P^{(s)}(t) = \frac{1}{2} U^{(s)T}(t)\, A^{(s)}\, U^{(s)}(t) \tag{1.4}$$

is strain energy of the sth brick;

$$W^{(s)}(t) = U^{(s)T}(t)\, Q^{(s)}(t) \tag{1.4}$$

is work of external forces acting on the surfaces of the sth brick;

$$V_{PT}(t) = \sum_{\gamma=1}^{\Gamma_\gamma} \left[\left(\mathbf{R}^{(\gamma)}\ \mathbf{L}^{(\gamma)}(t) \right)^T \mathbf{U}^{(\gamma)}(t) - \left(\mathbf{L}^{(\gamma)}(t) \right)^T \mathbf{F}^{(\gamma)} - U_p(t)\, \mathbf{S}^{(\gamma)T}\, \mathbf{L}^{(\gamma)}(t) \right] \tag{1.5}$$

is the "projectile-target interactive term", the index γ denotes those bricks of the target which are in contact with projectile, and $U^{(\gamma)}(t)$ is the vector of unknown approximation coefficients corresponding to the normal displacements of the upper surfaces of those bricks which are exposed to the contact pressure. $L^{(\gamma)}(t)$ is the unknown vector whose components are the approximation coefficients of the Lagrange multiplier functions (these depend on time and in-plane coordinates x and y).

Explicit forms of vectors $\mathbf{U}^{(s)}$, $\mathbf{Q}^{(s)}$ and matrices $\mathbf{A}^{(s)}$, $\mathbf{M}^{(s)}$ are given by equations (1.12) of Report [2]. Explicit forms of the vectors $\mathbf{U}^{(\gamma)}$, $\mathbf{L}^{(\gamma)}$, $\mathbf{F}^{(\gamma)}$, $\mathbf{S}^{(\gamma)}$, and the matrix $\mathbf{R}^{(\gamma)}$ are given by equations (2.21) of Report [2]. Let us introduce the following vectors and matrices:

$$\mathbf{U} = \begin{Bmatrix} \mathbf{U}^{(1)} \\ \cdots \\ \mathbf{U}^{(S)} \end{Bmatrix}, \mathbf{Q} = \begin{Bmatrix} \mathbf{Q}^{(1)} \\ \cdots \\ \mathbf{Q}^{(S)} \end{Bmatrix}, \quad \mathbf{A} = \begin{bmatrix} \mathbf{A}^{(1)} & 0 & \cdots & 0 \\ 0 & \mathbf{A}^{(2)} & \cdots & 0 \\ \cdots & \cdots & \cdots & \cdots \\ 0 & 0 & \cdots & \mathbf{A}^{(S)} \end{bmatrix}, \mathbf{M} = \begin{bmatrix} \mathbf{M}^{(1)} & 0 & \cdots & 0 \\ 0 & \mathbf{M}^{(2)} & \cdots & 0 \\ \cdots & \cdots & \cdots & \cdots \\ 0 & 0 & \cdots & \mathbf{M}^{(S)} \end{bmatrix} \tag{1.6}$$

$$\mathbf{U}_c = \begin{Bmatrix} \mathbf{U}^{(\gamma_1)} \\ \cdots \\ \mathbf{U}^{(\gamma_\Gamma)} \end{Bmatrix}, \mathbf{L} = \begin{Bmatrix} \mathbf{L}^{(\gamma_1)} \\ \cdots \\ \mathbf{L}^{(\gamma_\Gamma)} \end{Bmatrix}, \mathbf{F} = \begin{Bmatrix} \mathbf{F}^{(\gamma_1)} \\ \cdots \\ \mathbf{F}^{(\gamma_\Gamma)} \end{Bmatrix}, \mathbf{S} = \begin{Bmatrix} \mathbf{S}^{(\gamma_1)} \\ \cdots \\ \mathbf{S}^{(\gamma_\Gamma)} \end{Bmatrix}, \mathbf{R} = \begin{bmatrix} \mathbf{R}^{(\gamma_1)} & 0 & \ldots & 0 \\ 0 & \mathbf{R}^{(\gamma_2)} & \ldots & 0 \\ \ldots & \ldots & \ldots & \ldots \\ 0 & 0 & \ldots & \mathbf{R}^{(\gamma_\Gamma)} \end{bmatrix} \tag{1.7}$$

It should be emphasized that all components of the vector $\mathbf{U}_c(t)$ are already present in the full set of displacement approximation coefficients of the vector $\mathbf{U}(t)$. Using the notations of (1.6) and (1.7), the Lagrangian function (1.2) can be written as

$$\mathbf{L} = \frac{1}{2}\dot{\mathbf{U}}_p \mathbf{M}_p \dot{\mathbf{U}}_p + \frac{1}{2}\dot{\mathbf{U}}^T \mathbf{M} \dot{\mathbf{U}} - \frac{1}{2}\dot{\mathbf{U}}^T \mathbf{A}\, \mathbf{U} + \mathbf{U}^T \mathbf{Q} + \mathbf{L}^T \mathbf{R}^T \mathbf{U}_c - \mathbf{L}^T \mathbf{F} - \mathbf{U}_p \mathbf{S}^T \mathbf{L} \tag{1.8}$$

The Lagrangian function (1.8) will be used in the next section for derivation of the equations of motion of the target and projectile.

1.2. COMPUTATIONAL ALGORITHM FOR DYNAMIC CONTACT ANALYSIS

The full set of unknown functions is represented by vector of undetermined displacement approximation coefficients of the target, $\mathbf{U}(t)$, vector of undetermined coefficients of the Lagrangian multipliers $\mathbf{L}(t)$, and projectile velocity $\dot{\mathbf{U}}_p(t)$. The full set of the displacement approximation coefficients of the target includes the subvector, $\mathbf{U}_c(t)$, which contains coefficients corresponding to those external surfaces of the mosaic body which are in contact with the projectile, and the subvector, $\mathbf{U}_f(t)$, which contains coefficients not related to the external surfaces of the mosaic body which are in contact with the projectile. Accordingly,

$$\mathbf{U}(t) = \mathbf{U}_c(t) \cup \mathbf{U}_f(t) \tag{1.9}$$

Due to the projectile-target non-penetration condition (see equation (2.24) of Report [2]), the components of subvector $\mathbf{U}_c(t)$ are not independent unknown functions. Therefore, the coefficients $\mathbf{U}_c(t)$ can be excluded from the resulting system of equations of motion. For this purpose, the vector $\mathbf{U}$ and the corresponding matrices $\mathbf{M}$, $\mathbf{A}$, and the loading vector $\mathbf{Q}$ are substructured as follows:

$$\mathbf{U}=\begin{Bmatrix}\mathbf{U}_f\\ \mathbf{U}_c\end{Bmatrix},\ \mathbf{M}=\begin{bmatrix}\mathbf{M}_{ff} & \mathbf{M}_{fc}\\ \mathbf{M}_{cf} & \mathbf{M}_{cc}\end{bmatrix},\ \mathbf{A}=\begin{bmatrix}\mathbf{A}_{ff} & \mathbf{A}_{fc}\\ \mathbf{A}_{cf} & \mathbf{A}_{cc}\end{bmatrix},\ \mathbf{Q}=\begin{Bmatrix}\mathbf{Q}_f\\ \mathbf{Q}_c\end{Bmatrix} \tag{1.10}$$

Using (1.10), the Lagrangian function (1.8) can be rewritten as

$$\mathbf{L}=\frac{1}{2}\begin{Bmatrix}\mathbf{U}_f\\ \mathbf{U}_c\\ \mathbf{L}\\ \mathbf{U}_p\end{Bmatrix}^T\begin{bmatrix}\mathbf{M}_{ff} & \mathbf{M}_{fc} & 0 & 0\\ \mathbf{M}_{cf} & \mathbf{M}_{cc} & 0 & 0\\ 0 & 0 & 0 & 0\\ 0 & 0 & 0 & \mathbf{M}_p\end{bmatrix}\begin{Bmatrix}\mathbf{U}_f\\ \mathbf{U}_c\\ \mathbf{L}\\ \mathbf{U}_p\end{Bmatrix}-\frac{1}{2}\begin{Bmatrix}\mathbf{U}_f\\ \mathbf{U}_c\\ \mathbf{L}\\ \mathbf{U}_p\end{Bmatrix}^T\begin{bmatrix}\mathbf{A}_{ff} & \mathbf{A}_{fc} & 0 & 0\\ \mathbf{A}_{cf} & \mathbf{A}_{cc} & 0 & 0\\ 0 & -2\mathbf{R} & 0 & 0\\ 0 & 0 & 2\mathbf{S} & 0\end{bmatrix}\begin{Bmatrix}\mathbf{U}_f\\ \mathbf{U}_c\\ \mathbf{L}\\ \mathbf{U}_p\end{Bmatrix}+$$

$$+\begin{Bmatrix}\mathbf{U}_f\\ \mathbf{U}_c\\ \mathbf{L}\\ \mathbf{U}_p\end{Bmatrix}^T\begin{Bmatrix}\mathbf{Q}_f\\ \mathbf{Q}_c\\ -\mathbf{F}\\ 0\end{Bmatrix} \tag{1.11}$$

Further, by introducing notations

$$\mathbf{A}_{Lc}=-\mathbf{R},\ \mathbf{A}_{PL}=2\mathbf{S},\ \mathbf{Q}_L=-\mathbf{F} \tag{1.12}$$

the Lagrangian function (1.11) takes the form

$$\mathbf{L}=\frac{1}{2}\begin{Bmatrix}\mathbf{U}_f\\ \mathbf{U}_c\\ \mathbf{L}\\ \mathbf{U}_p\end{Bmatrix}^T\begin{bmatrix}\mathbf{M}_{ff} & \mathbf{M}_{fc} & 0 & 0\\ \mathbf{M}_{cf} & \mathbf{M}_{cc} & 0 & 0\\ 0 & 0 & 0 & 0\\ 0 & 0 & 0 & \mathbf{M}_p\end{bmatrix}\begin{Bmatrix}\mathbf{U}_f\\ \mathbf{U}_c\\ \mathbf{L}\\ \mathbf{U}_p\end{Bmatrix}-\frac{1}{2}\begin{Bmatrix}\mathbf{U}_f\\ \mathbf{U}_c\\ \mathbf{L}\\ \mathbf{U}_p\end{Bmatrix}^T\begin{bmatrix}\mathbf{A}_{ff} & \mathbf{A}_{fc} & 0 & 0\\ \mathbf{A}_{cf} & \mathbf{A}_{cc} & 0 & 0\\ 0 & \mathbf{A}_{Lc} & 0 & 0\\ 0 & 0 & \mathbf{A}_{FL} & 0\end{bmatrix}\begin{Bmatrix}\mathbf{U}_f\\ \mathbf{U}_c\\ \mathbf{L}\\ \mathbf{U}_p\end{Bmatrix}+$$

$$+\begin{Bmatrix}\mathbf{U}_f\\ \mathbf{U}_c\\ \mathbf{L}\\ \mathbf{U}_p\end{Bmatrix}^T\begin{Bmatrix}\mathbf{Q}_f\\ \mathbf{Q}_c\\ -\mathbf{F}\\ 0\end{Bmatrix} \tag{1.13}$$

After applying the Lagrange equations

$$\frac{d}{dt}\left(\frac{\partial \mathbf{L}}{\partial \dot{\mathbf{U}}_f}\right)-\frac{\partial \mathbf{L}}{\partial \mathbf{U}_f}=0,\quad \frac{d}{dt}\left(\frac{\partial \mathbf{L}}{\partial \dot{\mathbf{U}}_c}\right)-\frac{\partial \mathbf{L}}{\partial \mathbf{U}_c}=0$$
$$\frac{d}{dt}\left(\frac{\partial \mathbf{L}}{\partial \dot{\mathbf{L}}}\right)-\frac{\partial \mathbf{L}}{\partial \mathbf{L}}=0,\quad \frac{d}{dt}\left(\frac{\partial \mathbf{L}}{\partial \dot{\mathbf{U}}_P}\right)-\frac{\partial \mathbf{L}}{\partial \mathbf{U}_P}=0 \tag{1.14}$$

to the Lagrange function (1.13) the following equations of the motion are derived:

$$\mathbf{M}_{ff}\frac{d^2\mathbf{U}_f}{dt^2}+\mathbf{M}_{fc}\frac{d^2\mathbf{U}_c}{dt^2}+\mathbf{A}_{ff}\mathbf{U}_f+\mathbf{A}_{fc}\mathbf{U}_c=\mathbf{Q}_f \tag{1.15}$$

$$\mathbf{M}_{cf}\frac{d^2\mathbf{U}_f}{dt^2}+\mathbf{M}_{cc}\frac{d^2\mathbf{U}_c}{dt^2}+\mathbf{A}_{cf}\mathbf{U}_f+\mathbf{A}_{cc}\mathbf{U}_c+\frac{1}{2}\mathbf{A}_{Lc}\mathbf{L}=\mathbf{Q}_c \tag{1.16}$$

$$\mathbf{A}_{Lc}\mathbf{U}_c+U_P\mathbf{A}_{PL}=2\mathbf{Q}_L \tag{1.17}$$

$$M_P\frac{d^2U_P}{dt^2}+\frac{1}{2}\mathbf{A}_{PL}\mathbf{L}=0 \tag{1.18}$$

Equation (1.17) can be solved for $\mathbf{U}_c$:

$$\mathbf{U}_c=-\mathbf{A}_{Lc}^{-1}\mathbf{A}_{PL}U_P+2\mathbf{A}_{Lc}^{-1}\mathbf{Q}_L=\mathbf{T}_c^{(1)}U_P+\mathbf{T}_c^{(0)} \tag{1.19}$$

where $\mathbf{T}_C^{(1)} = -\mathbf{A}_{LC}^{-1}\mathbf{A}_{PL}$ and $\mathbf{T}_C^{(0)} = 2\,\mathbf{A}_{LC}^{-1}\mathbf{Q}_L$. It can be shown that $\mathbf{T}_C^{(1)} \equiv 1$ and $\mathbf{T}_C^{(0)} \equiv 0$ for the particular case of flat projectile. Substitution (1.19) into (1.15) and (1.16) yields:

$$\mathbf{M}_{ff}\frac{d^2\mathbf{U}_f}{dt^2}-\mathbf{M}_{fc}\mathbf{T}_c^{(1)}\mathbf{A}_{PL}\frac{d^2U_P}{dt^2}+\mathbf{A}_{ff}\mathbf{U}_f+\mathbf{A}_{fc}\mathbf{T}_c^{(1)}U_P=\mathbf{Q}_f-\mathbf{A}_{fc}\mathbf{T}_c^{(0)} \tag{1.20}$$

$$\mathbf{M}_{cf}\frac{d^2\mathbf{U}_f}{dt^2}+\mathbf{M}_{cc}\mathbf{T}_c^{(1)}\frac{d^2U_P}{dt^2}+\mathbf{A}_{cf}\mathbf{U}_f+\mathbf{A}_{cc}\mathbf{T}_c^{(1)}U_P+\frac{1}{2}\mathbf{A}_{Lc}\mathbf{L}=\mathbf{Q}_c-\mathbf{A}_{cc}\mathbf{T}_c^{(0)} \tag{1.21}$$

Equation (1.21) can be further solved for **L**:

$$\mathbf{L}=2\left(\mathbf{P}_{cf}^{(2)}\frac{d^2\mathbf{U}_f}{dt^2}+\mathbf{P}_c^{(2)}\frac{d^2U_P}{dt^2}+\mathbf{P}_{cf}^{(1)}\mathbf{U}_f+\mathbf{P}_c^{(1)}U_P+\mathbf{P}_c^{(0)}\right) \tag{1.22}$$

where

$$\begin{aligned}&\mathbf{P}_{cf}^{(2)}=-\mathbf{A}_{Lc}^{-1}\mathbf{M}_{cf}, \qquad \mathbf{P}_{cf}^{(1)}=-\mathbf{A}_{Lc}^{-1}\mathbf{A}_{cf},\\ &\mathbf{P}_c^{(2)}=-\mathbf{A}_{Lc}^{-1}\mathbf{M}_{cc}\mathbf{T}_c^{(1)}, \quad \mathbf{P}_c^{(1)}=-\mathbf{A}_{Lc}^{-1}\mathbf{A}_{cc}\mathbf{T}_c^{(1)}, \quad \mathbf{P}_c^{(0)}=\mathbf{A}_{Lc}^{-1}\mathbf{Q}_c-\mathbf{A}_{Lc}^{-1}\mathbf{A}_{cc}\mathbf{T}_c^{(0)}\end{aligned} \tag{1.23}$$

Finally, substituting (1.22) into (1.18) yields:

$$\left(M_P+\mathbf{A}_{PL}\mathbf{P}_c^{(2)}\right)\frac{d^2U_P}{dt^2}+\mathbf{A}_{PL}\mathbf{P}_{cf}^{(2)}\frac{d^2\mathbf{U}_f}{dt^2}+\mathbf{A}_{PL}\mathbf{P}_{cf}^{(1)}\mathbf{U}_f+\mathbf{A}_{PL}\mathbf{P}_c^{(1)}U_P+\mathbf{A}_{PL}\mathbf{P}_c^{(0)}=0 \tag{1.24}$$

The resulting system of equations (1.20) and (1.24) can be written in a compact matrix form as following

$$\begin{bmatrix} \mathbf{M}_{ff} & \mathbf{M}_{fc}\mathbf{T}_c^{(1)} \\ \mathbf{A}_{PL}\mathbf{P}_{cf}^{(2)} & \left(M_P + \mathbf{A}_{PL}\mathbf{P}_c^{(2)}\right) \end{bmatrix} \begin{Bmatrix} \ddot{\mathbf{U}}_f \\ \ddot{U}_P \end{Bmatrix} + \begin{bmatrix} \mathbf{A}_{ff} & \mathbf{A}_{fc}\mathbf{T}_c^{(1)} \\ \mathbf{A}_{PL}\mathbf{P}_{cf}^{(1)} & \mathbf{A}_{PL}\mathbf{P}_c^{(1)} \end{bmatrix} \begin{Bmatrix} \mathbf{U}_f \\ U_P \end{Bmatrix} = \begin{Bmatrix} \mathbf{Q}_f - \mathbf{A}_{fc}\mathbf{T}_c^{(0)} \\ -\mathbf{A}_{PL}\mathbf{P}_c^{(0)} \end{Bmatrix} \tag{1.25}$$

The following initial conditions are added

$$\mathbf{U}_f\Big|_{t=0} = \frac{d\mathbf{U}_f}{dt}\Big|_{t=0} = 0 \tag{1.26}$$

$$U_P\Big|_{t=0} = 0, \quad \frac{dU_P}{dt}\Big|_{t=0} = -V_0 \tag{1.27}$$

Here, V_0 is initial velocity of the projectile.

Once the system of linear ordinary differential equations (1.25) is solved, the rest of unknown displacement approximation coefficients $\mathbf{U}_c$ is evaluated using relation (1.19) and the coefficients $\mathbf{L}$ of the Lagrange multiplier functions are evaluated using relation (1.22).

Several numerical examples illustrating application of the developed analysis approach are presented in the next sections.

2. NUMERICAL EXAMPLES

2.1. Transverse dynamic bending of [0°/90°/0°] simply supported plate

In order to verify accuracy of the developed computational algorithm and computer code, consider first the problem of dynamic transverse bending of a simply supported 3-layer [0°/90°/0°] rectangular plate having length a, width b and thickness h, as ilustrated in Figure 2.1. The external surface load, q(x,y,t), is assumed to be distributed as a double-sine function over the top surface of the plate:

$$q(x,y,t) = q_0(t)\sin\left(\frac{\pi x}{a}\right)\sin\left(\frac{\pi y}{b}\right) \tag{2.1}$$

The following kinematic boundary conditions are imposed:

$$(u_y)_{x=0} = (u_y)_{x=a} = (u_z)_{x=0} = (u_z)_{x=a} = 0 \tag{2.2}$$

$$(u_x)_{y=0} = (u_x)_{y=b} = (u_z)_{y=0} = (u_z)_{y=b} = 0 \tag{2.3}$$

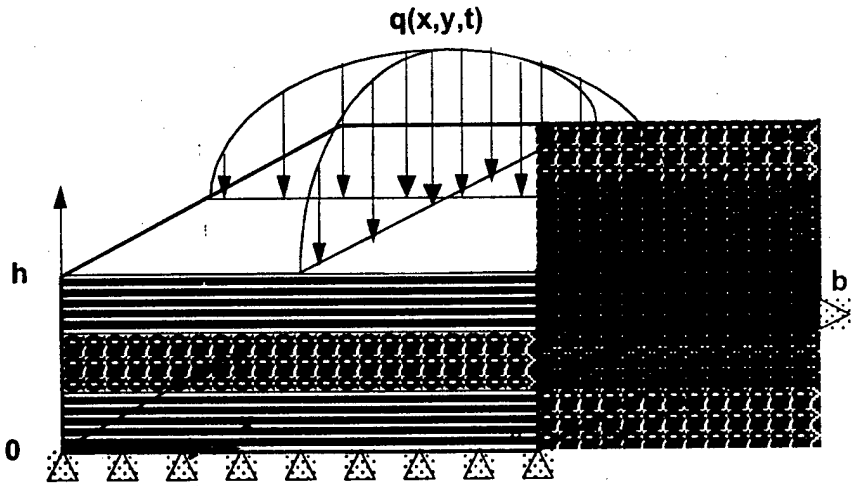

Figure 2.1. Schematic of transverse dynamic bending of simply supported laminated plate.

The initial conditions are of the form

$$(u_x)_{t=0} = (u_y)_{t=0} = (u_z)_{t=0} = \left(\frac{\partial u_x}{\partial t}\right)_{t=0} = \left(\frac{\partial u_y}{\partial t}\right)_{t=0} = \left(\frac{\partial u_z}{\partial t}\right)_{t=0} = 0 \tag{2.4}$$

The loading condition

$$(\sigma_z)_{z=h} = q(x,y,t) \tag{2.5}$$

is not imposed, but is expected to be satisfied as a "natural" boundary condition at any time instant during the loading history. Components of the external force vector $Q^{(s)}(t)$ entering in expression (1.4) for the work of external forces acting on the surfaces of the sth brick are obtained as following

$$Q_{ijk}^{\alpha(s)}(t) = \begin{cases} q_0(t)\int_0^a\int_0^b B_i^I(x)B_j^J(y)\sin\frac{\pi x}{a}\sin\frac{\pi y}{b}dxdy \ \text{for}\ \alpha=3,\ s=3,\ i=1,\ldots I,\ j=1,\ldots J,\ k=K \\ 0 \quad else \end{cases} \tag{2.6}$$

where $B_i^I(x)$ and $B_j^J(x)$ are Bernstein basis functions.

The normalized time variable

$$\tau = t/t_0 \tag{2.7}$$

is used in all forthcoming plots. The parameter t_0 is the time required for the transverse stress wave to travel through the thickness of the plate. This time is defined as

$$t0 = h\sqrt{\frac{E_L\,(1-\nu_{TT})}{\rho\,(1-\nu_{TT}-2\nu_{TL}\nu_{LT})}} \tag{2.8}$$

The applied surface load is a linear function on time:

$$q_0(t) = \sigma\,\tau/\tau_0 \tag{2.9}$$

where σ is a constant and parameter τ_0 defines the loading rate. The dynamic solution should approach the corresponding quasi-static solution as τ_0 increases.

Material properties and the displacement and stress normalization factors are taken as in [3]:

$$(\bar{\sigma}_x,\bar{\sigma}_y,\bar{\tau}_{xy}) = \frac{1}{\sigma S^2}(\sigma_x,\sigma_y,\tau_{xy}), \qquad \bar{\sigma}_z = \frac{\sigma_z}{\sigma}$$

$$(\bar{\tau}_{xz},\bar{\tau}_{yz}) = \frac{1}{\sigma S}(\tau_{xz},\tau_{yz})$$

$$(\bar{u}_x, \bar{u}_y) = \frac{E_T}{\sigma h S^3}(u_x, u_y), \qquad (2.10)$$

$$\bar{u}_z = \frac{100 E_T}{\sigma h S^4} u_z \qquad S = a/h$$

The example considered here corresponds to a=b, S=4.

In this analysis, just one brick is taken within each layer of the plate. Hence, total number of bricks is 3, and L=1, M=1, N=3. Sixth degree Bernstein basis functions are used in all coordinate directions, I=J=K=6.

Variations in time of the normal displacement and stresses at various loading rates are presented in Figs. 2.2-2.6. Fig. 2.2 shows that the normal stress $\bar{\sigma}_z$ at the top surface of the plate is equal to the applied load at any time instant during loading history. Thus, loading condition (2.5) is satisfied with high accuracy. Fig. 2.6 shows that dynamic displacements and stresses oscillate about the corresponding quasi-static values (shown by dotted line). At a comparatively low loading rates ($\tau_0 \geq 5$), dynamic displacements and stresses reach the corresponding static values at time instant $\tau = \tau_0$, when the dynamic load reaches static load level σ. However, at a comparatively high loading rates ($\tau_0 \leq 2$) dynamic displacements and stresses at $\tau = \tau_0$ are lower than the corresponding static values. This effect manifests the well-known effect that a delay in dynamic structural response is increasing at higher loading rates.

Additional comparisons are presented in Table 2.1. Here, the benchmark of Pagano's static solution results [3] are presented together with numerical results of our 3-D static solution (see, Report [4] for details), and present dynamic solution. In the latter one, the stresses are evaluated at $\tau = \tau_0$ for various loading rates. It is seen from this Table that the dynamic stresses approach their respective static values as loading rate decreases. However, there is still small difference (about 0.3% for $\tau_0 = 0$) between the computed dynamic stresses and the corresponding static stresses for the lowest loading rate under consideration. This difference may be explained by the oscillatory character of the dynamic solution. According to Fig. 2.6, the amplitude of the stress oscillation is 0.35%, which is larger than the difference between the obtained dynamic solutions at the lowest loading rate and the corresponding quasi-static solution.

Distributions of the stresses and displacement through the thickness of the plate are sown in Figs. 2.7-2.10. It is seen that the shapes of dynamical stress distributions are exactly the same as the shapes of the corresponding static stress distributions.

The considered numerical example validates the computational algorithm and computer code for the dynamic analysis of laminated composite plates.

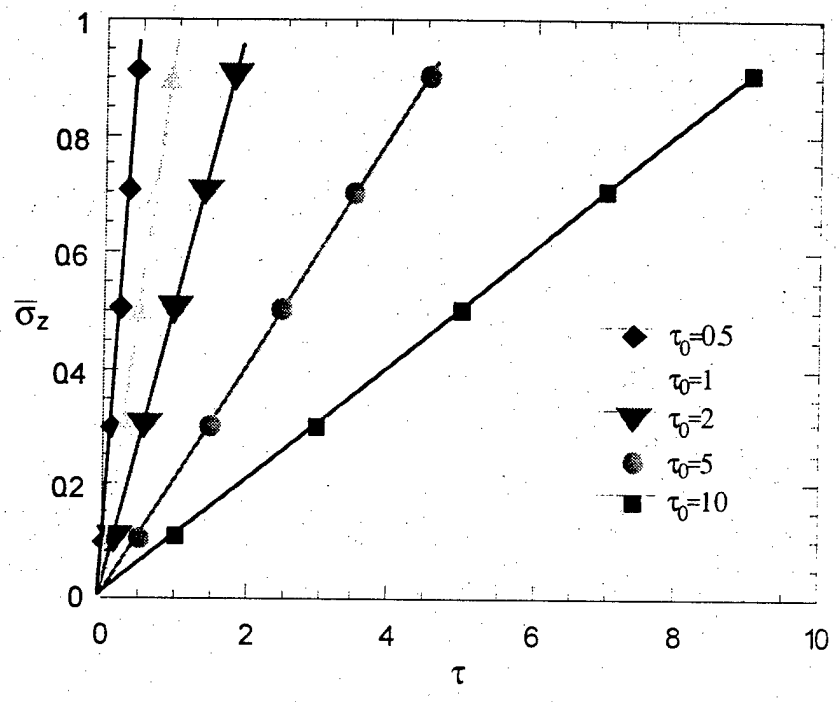

Figure 2.2. Variation in time of the normal stress $\bar{\sigma}_z$ at x=a/2, y=b/2, z=h for various loading rates.

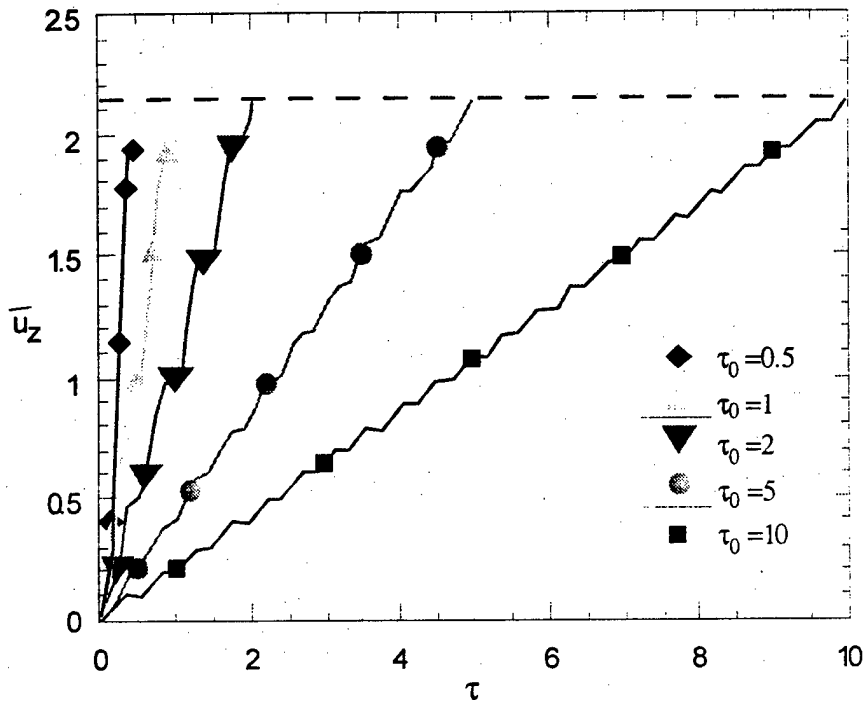

Figure 2.3. Variation in time of the normal displacement $\overline{u}_z$ at x=a/2, y=b/2, z=h for various loading rates. The dashed line corresponds to the static solution.

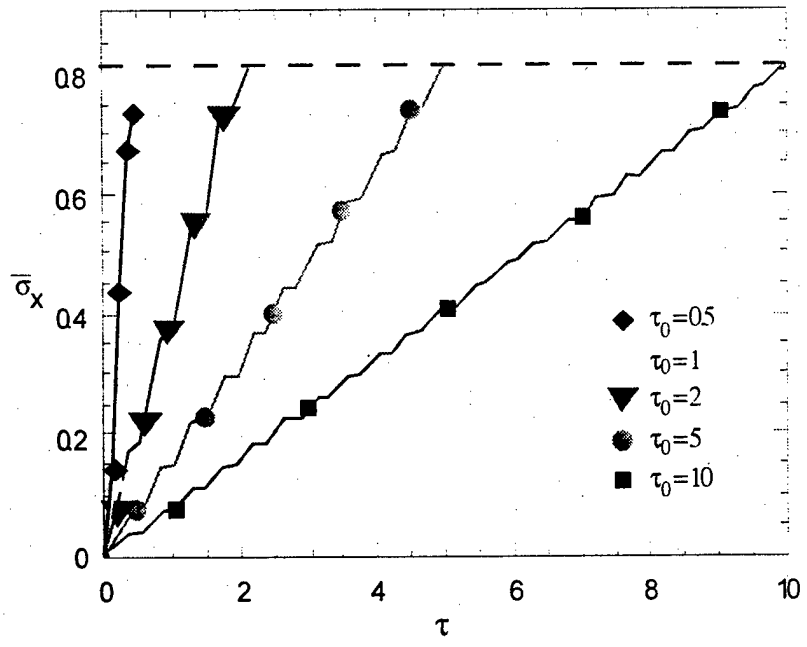

Figure 2.4. Variation in time of the normal stress $\overline{\sigma}_x$ at x=a/2, y=b/2, z=h for various loading rates. Dashed line corresponds to the static solution.

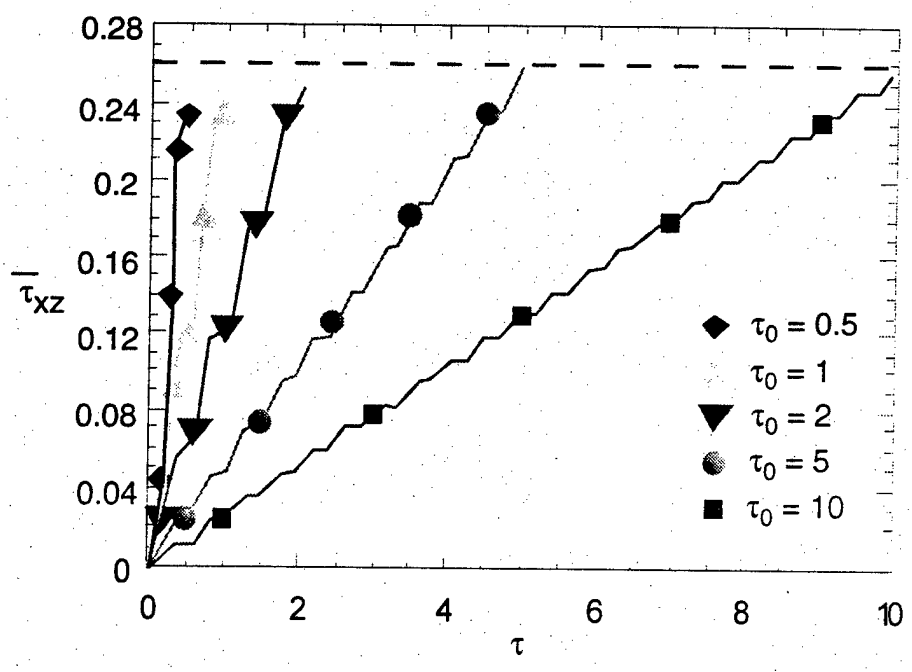

Figure 2.5. Variation in time of the shear stress $\bar{\tau}_{xz}$ at x=0, y=b/2, z=h/2 for various loading rates. Dashed line corresponds to the static solution.

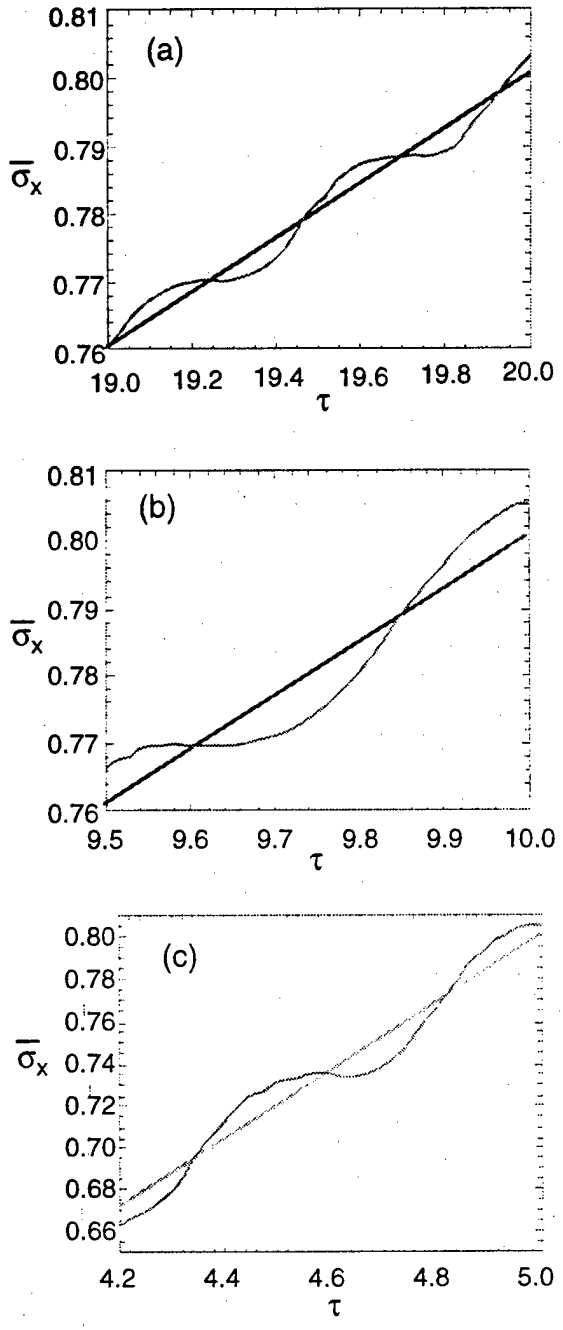

Figure 2.6. Variation in time of the normal stress $\overline{\sigma}_x$ at x=a/2, y=b/2, z=h for loading rates τ_0=5 (a), 10 (b), and 20 (c). Red lines correspond to quasi-static solution.

Table 2.1. Comparison between present dynamic and static results and the static results from [3] for the case of [0°/90°/0°] square plate with a/h=4.

Reference	$\bar{\sigma}_x\left(\frac{a}{2},\frac{b}{2},h\right)$	$\bar{\sigma}_x\left(\frac{a}{2},\frac{b}{2},0\right)$	$\bar{\sigma}_y\left(\frac{a}{2},\frac{b}{2},\frac{2h}{3}\right)$	$\bar{\sigma}_y\left(\frac{a}{2},\frac{b}{2},\frac{2h}{3}\right)$	$\bar{\tau}_{xy}(0.0,h)$	$\bar{\tau}_{xz}\left(0,\frac{b}{2},\frac{h}{2}\right)$	$\bar{\tau}_{yz}\left(\frac{a}{2},0,\frac{h}{2}\right)$
Static [3]	0.801	-0.755	0.534	-0.556	-0.0511	0.256	0.2172
Static present	0.8005	-0.7545	0.5339	-0.5560	-0.0511	0.2559	0.2172
Dynamic, τ_0=0.5	0.7377	-0.6942	0.4899	-0.5114	-0.04687	0.2352	0.2004
Dynamic, τ_0=1	0.7489	-0.7031	0.4959	-0.5185	-0.04758	0.2387	0.2034
Dynamic, τ_0=2	0.7794	-0.7340	0.5184	-0.5406	-0.04962	0.2491	0.2117
Dynamic, τ_0=5	0.8060	-0.7601	0.5381	-0.5612	-0.05146	0.2578	0.2186
Dynamic, τ_0=10	0.8053	-0.7593	0.5375	-0.5596	-0.05140	0.2575	0.2185
Dynamic, τ_0=20	0.8029	-0.7569	0.5357	-0.5578	-0.05124	0.2567	0.2178

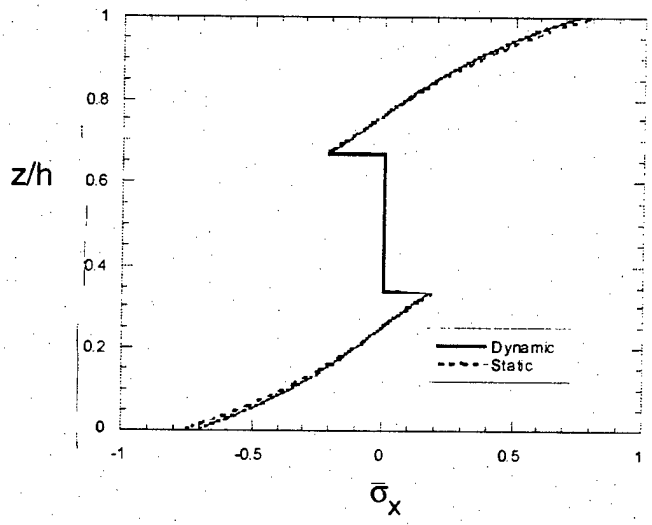

Figure 2.7. Normal stress distribution at x=a/2, y=b/2. Dynamic solution corresponds to loading rate τ_0 = 1.

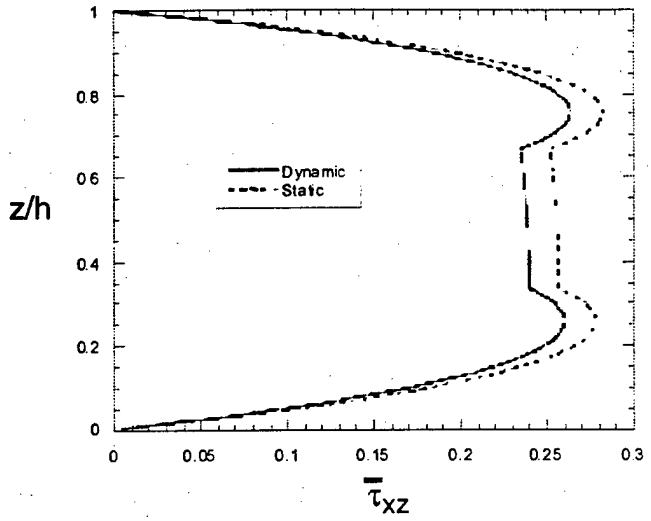

Figure 2.8. Transverse shear stress distribution at x=0, y=b/2. Dynamic solution corresponds to loading rate $\tau_0 = 1$.

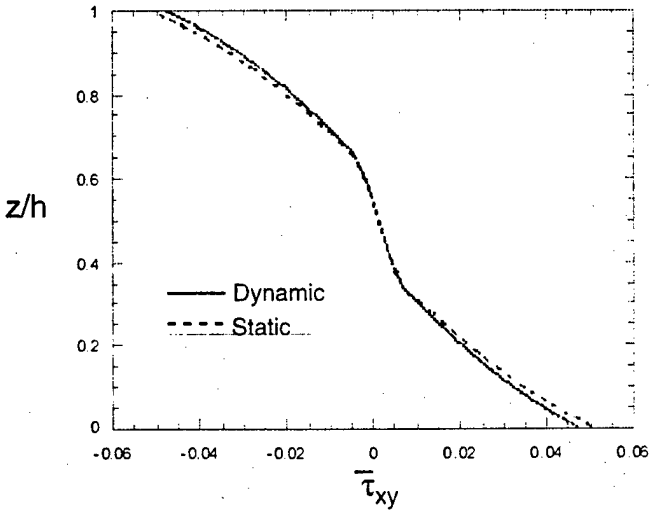

Figure 2.9. In-plane shear stress distribution at x=0, y=0. Dynamic solution corresponds to loading rate τ_0=1.

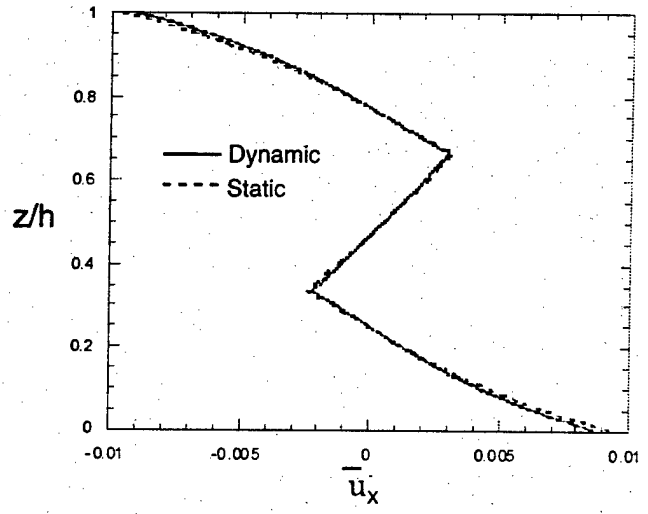

Figure 2.10. The in-plane displacement distribution at x=0, y=b/2. Dynamic solution corresponds to loading rate τ_0=1.

2.2. LONGITUDINAL 3D Impact Contact Analysis of multi-brick structures

3-D impact contact analysis of prismatic bar fully clamped at its bottom end and exposed to a rigid mass longitudinal impact at the upper end was considered in the previous interim Report [2]. Schematic of the problem is shown in Fig. 2.11a. This analysis case will be further referred as Case I. In order to validate the developed computational algorithm and computer code for the case of a multi-brick structure in the *x-y* plane, next illustrative example will consider impact contact analysis of a prismatic aluminum bar surrounded by solid bricks of a "soft" material, as shown in Fig. 2.11b. This analysis case is further referenced as Case II.

The purpose of this illustrative example is twofold. First, it is necessary to validate that the developed algorithm is capable of solving the impact contact problem for a mosaic body composed from very distinct material bricks. Second, the analysis results for the Cases I and II should be, ideally, indistinguishable, if the elastic modulus of the soft material, E'', is negligible compared to the elastic modulus of aluminum, E_{Al}. The other extreme case is if E'' is equal to E_{Al}. Then we have the problem of transverse impact on a homogeneous plate by a flat rectangular rigid projectile. Thus, the problem illustrated

in Fig. 2.11b for aluminum bar surrounded by bricks of soft material can be considered as the test case aimed at verification of the developed algorithm and computer code for the class of impact contact problems.

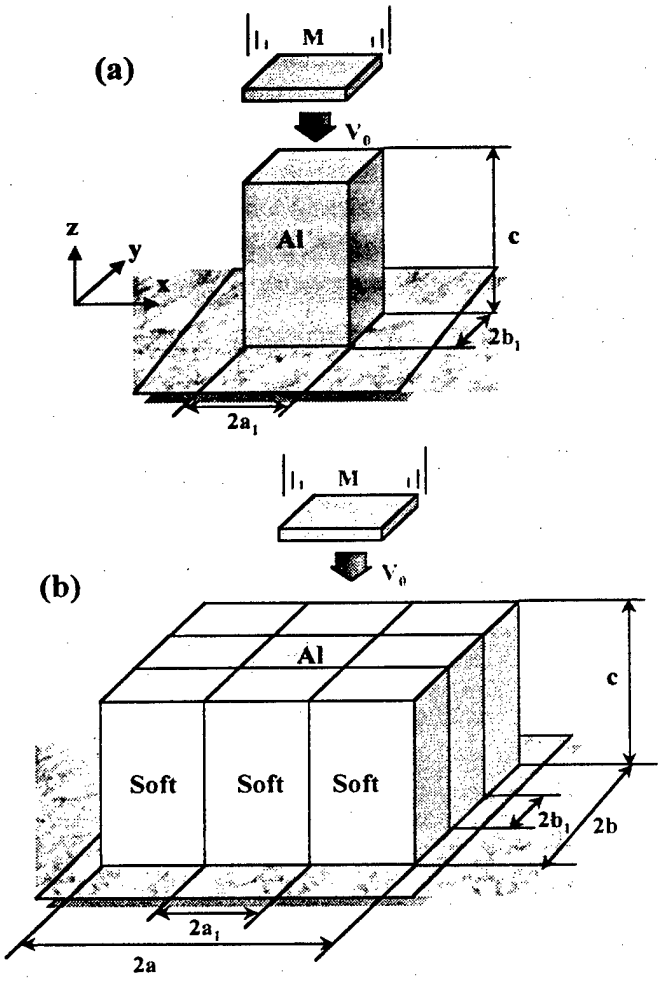

Figure 2.11. Impact contact analysis of aluminum bar (a) and aluminum bar surrounded by bricks of a "soft" material (b).

Due to the symmetry of the problem, we can analyze 1/4 of the full mosaic body, as shown in Fig. 2.12a. The regions considered are defined as following for Cases I and II:

$$\text{Case I:}\quad \begin{matrix} 0 \le x \le a_1 \\ 0 \le y \le b_1 \\ 0 \le z \le c \end{matrix} \qquad \text{Case II:}\quad \begin{matrix} 0 \le x \le a \\ 0 \le y \le b \\ 0 \le z \le c \end{matrix}$$

External kinematic boundary conditions are taken as follows

$$u_\alpha(x,y,z,t)\big|_{z=0} = 0, \quad \alpha = 1,2,3 \tag{2.11}$$

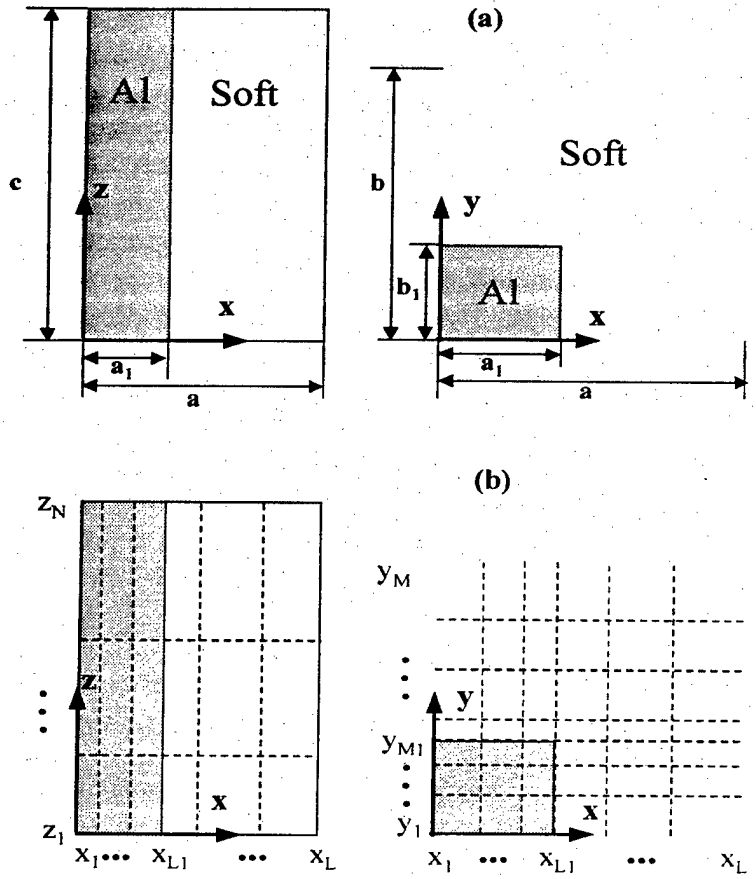

Figure 2.12. Geometry of $1/4^{th}$ part of aluminum bar surrounded by soft material (a) and schematic of the brick mesh (b).

and are complemented by the following symmetry conditions

$$\begin{aligned} u_1(x,y,z,t)\big|_{x=0} &= 0 \\ u_2(x,y,z,t)\big|_{y=0} &= 0 \end{aligned} \tag{2.12}$$

The initial conditions are formulated as

$$u_\alpha(x,y,z,t)\big|_{t=0} = \left.\frac{fu_\alpha(x,y,z,t)}{ft}\right|_{t=0} = 0, \quad \alpha = 1,2,3 \tag{2.13}$$

$$U(t) = 0, \quad \left.\frac{dU(t)}{dt}\right|_{t=0} = -V_0 \text{ , where } V_0 > 0 \tag{2.14}$$

The following material properties of Al bar are used:

$$E_{Al} = 73\ GPa,\quad \nu_{Al} = 0.3,\quad \rho_{Al} = 2.7?10^{3}\ \ kg/m^{3} \tag{2.15}$$

The geometric parameters are:

$$\begin{aligned} &a_1 = b_1 = 0.1\ m,\quad c = 0.2\ m \\ &a = 2a_1\quad b = 2b_1 \end{aligned} \tag{2.16}$$

Mass and velocity of the projectile are

$$M = 90\ kg,\quad V_0 = 12.5\ m/\sec \tag{2.17}$$

The following normalized time variable will be used:

$$\tau = t/t_0 \tag{2.18}$$

Here, parameter t_0 is defined as

$$t_0 = c_{Al}\left(\frac{E_{Al}(1-\nu_{Al})}{\rho_{Al}(1+\nu_{Al})(1-2\nu_{Al})}\right)^{-1/2} \approx 32\ \mu\sec \tag{2.19}$$

Numerical simulation results for the Cases I and II are presented in Figs. 2.13-2.15. Young's modulus of the soft material is taken four orders of magnitude lower than that of aluminum bar: $E^{*} = E_{Al}/10^{4}$.

Numerical results have been obtained with third degree Bernstein basis functions used for the three coordinate directions. Case I was simulated using a single brick in the x- and y-directions, and two bricks in the z-direction. In Case II three bricks were taken in the x-direction, three bricks in the y-direction, and two bricks in the z-direction. Using the notations introduced in Fig.2.12b, parameters of the brick mesh for Case II are:

$$\begin{aligned} &x_{L1} = a_1,\quad x_L = a; \qquad L1 = 2,\quad L = 4 \\ &y_{M1} = b_1,\quad y_M = b; \qquad M1 = 2,\quad M = 4 \\ &z_N = c;\ N = 3 \end{aligned} \tag{2.20}$$

Variation of the transverse displacement at the center point of the bar on its top surface $(x = y = 0,\ z = c)$ is shown in Fig. 2.13a. The displacement monotonically increases up

to $\tau \cup 8$, when the projectile moves downward. Then, the displacement monotonically decreases, following movement of the projectile upward to the time moment when the bar and projectile separate.

Distribution of the transverse displacement in the x-direction at y=0 z=c and time instant τ=5 is presented in Fig. 2.13b. It is seen that the displacement is uniformly distributed along the contact area, what is consistent with the assumption that the projectile is a flat rigid body. This figure also shows that the displacement continuity condition at the interface between the bar and soft material is satisfied exactly. At some distance away from the projectile, the displacement in a soft material tends to zero.

Variation of the projectile velocity on time is shown in Fig. 2.14. The velocity decreases from its initial value to zero (at $\tau \approx 8$), then increases and almost reaches its initial value.

Results presented in Figs. 2.13 and 2.14 indicate that there is no visible difference between results obtained for the Cases I and II when predicting variations of the transverse displacement and velocity of the projectile.

Time variations of the transverse normal strain in a bar and contact pressure are shown in Figs. 2.15 and 2.16. It is seen that the normal strains and contact pressure predicted for the Cases I and II are almost identical during the initial stage of impact. A minor discrepancy between these results is seen at the advanced stage of contact interaction; this can be explained by the effect of multiple stress wave reflections and from the external surfaces of the soft material in Case II.

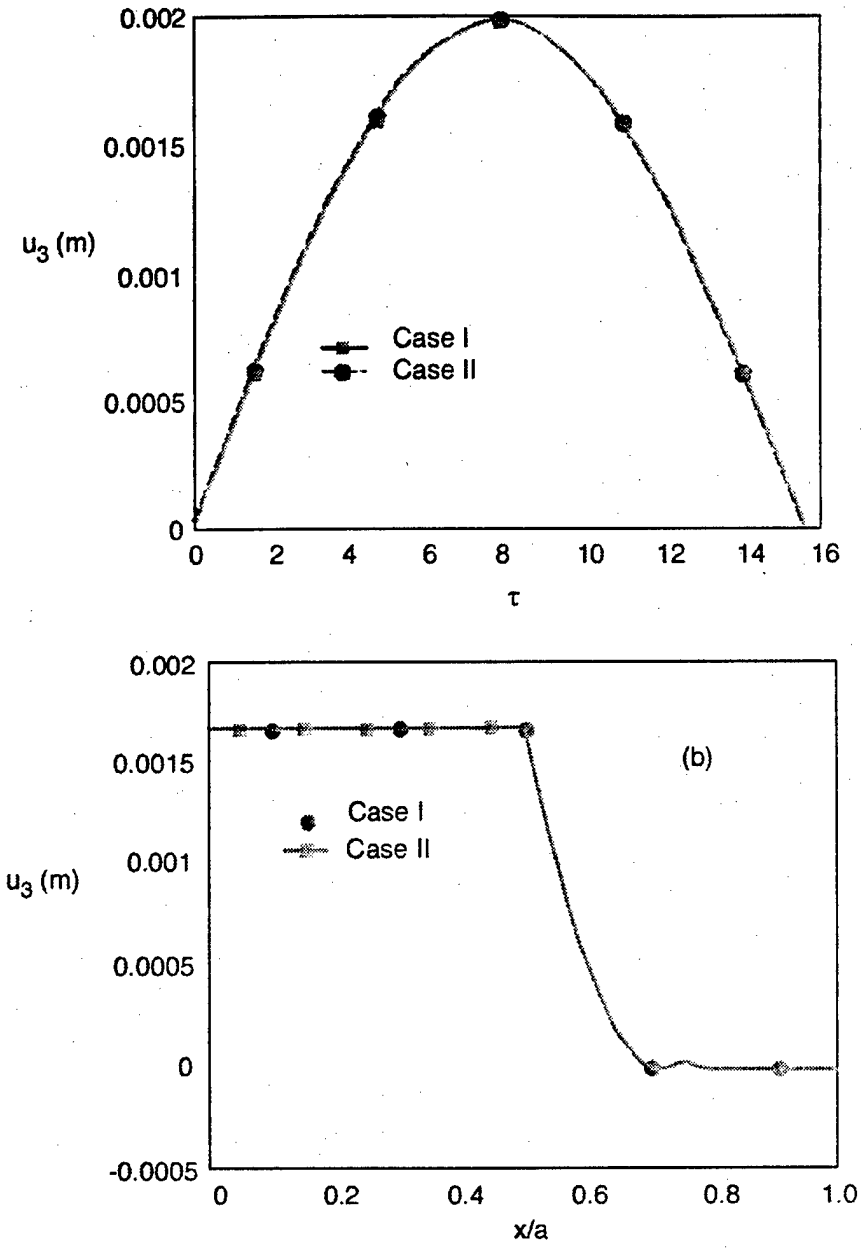

Fig. 2.13. Variations of the transverse displacement, u_3, in time (a) at x=y=0 and z=c, and its variation along the x-coordinate at y=0, z=c, τ=5 (b).

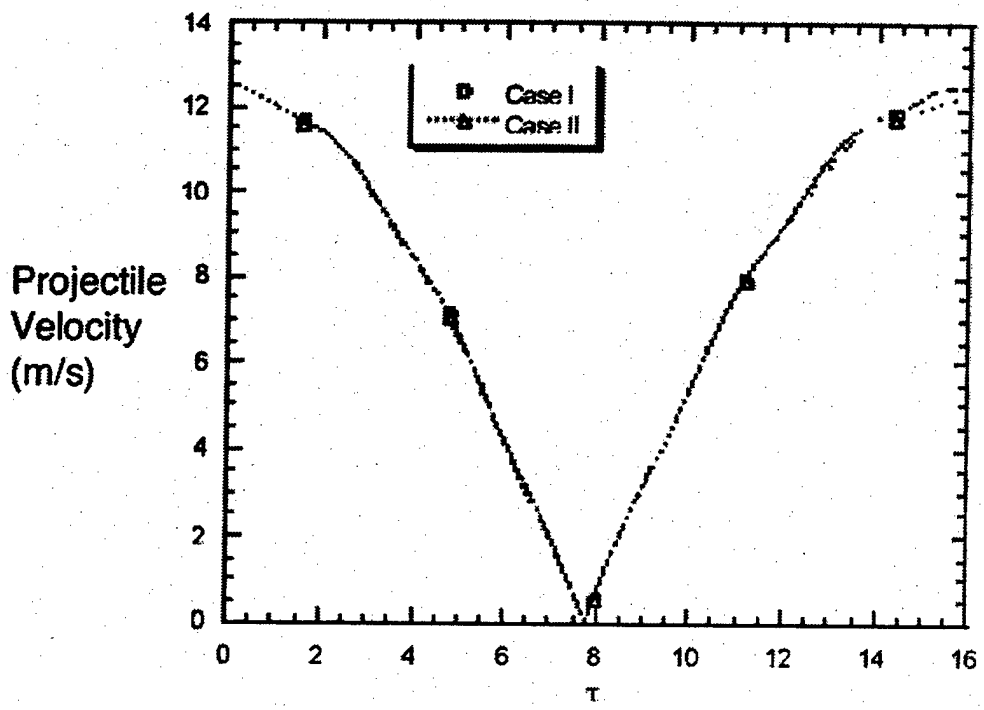

Fig. 2.14. Variation of the projectile velocity in time.

The dependence of the contact pressure on time shown in Fig. 2.16 indicates that the loss of contact between the bar and projectile occurs at $\tau \approx 16$. At this time instant velocity of the projectile approaches its initial value (the projectile moves upward, see Fig. 2.14). The observed short-period oscillations of the contact pressure are related to the stress waves reflections from external surfaces of the aluminum bar.

The above numerical examples verify that the developed algorithm and computer code provide accurate results for the considered 3-D impact contact problem with multiple bricks in the cross-section of the longitudinally impacted body. Next numerical study is carried out for the transverse impact contact analysis of thick aluminum plate.

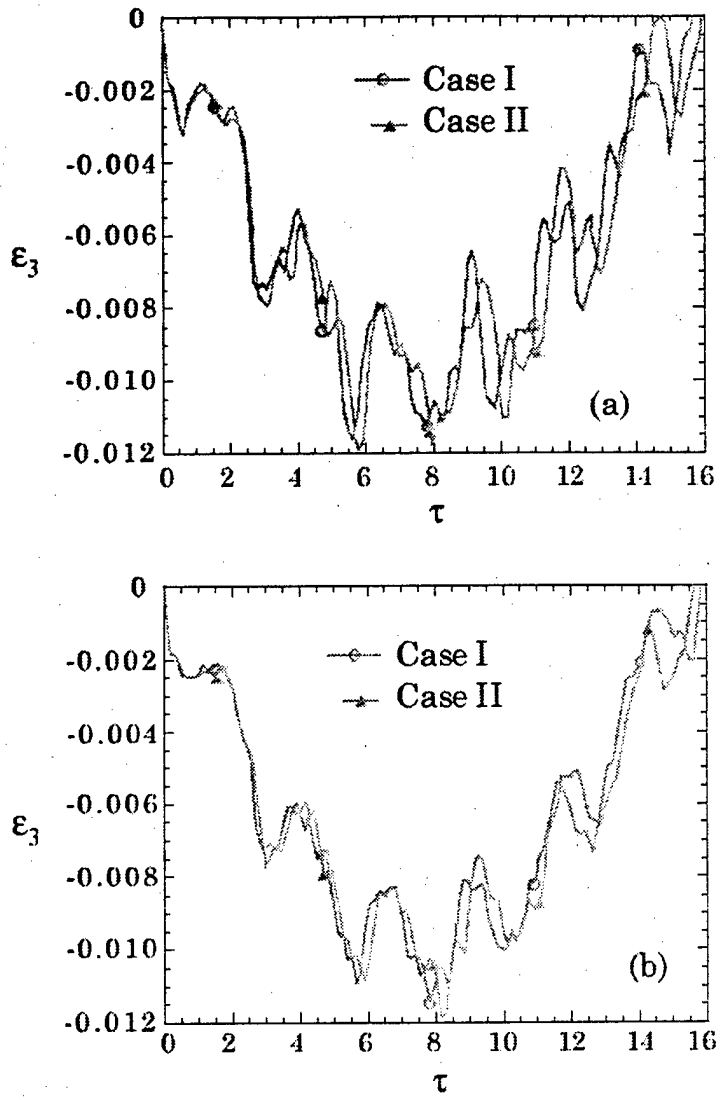

Fig. 2.15. Variation of the transverse strain ε_3 in time at $x = 0$ (a), and at $x = a/2$ (b); $y = 0$, $z = c$.

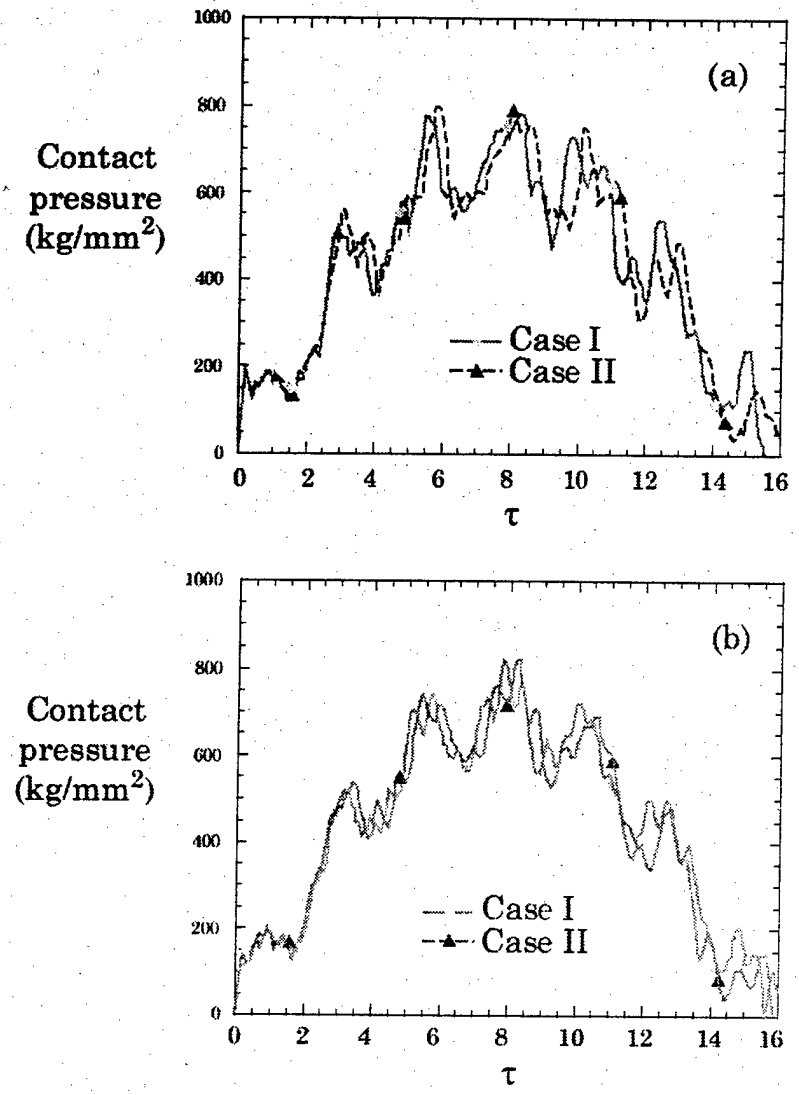

Fig.2.16. Variation of the contact pressure in time at x=0 (a), and at x=a/2 (b); y=0, z=c.

2.3. Transverse Impact Contact Analysis with Assumed Contact Zone

Consider another impact contact problem for a thick aluminum plate with dimensions a×b×c, as shown in Fig. 2.16. Dimensions of the projectile are $a_1 \times b_1$. Numerical values of the geometric parameters are defined by (2.16). Mass and velocity of the projectile are specified by (2.17).

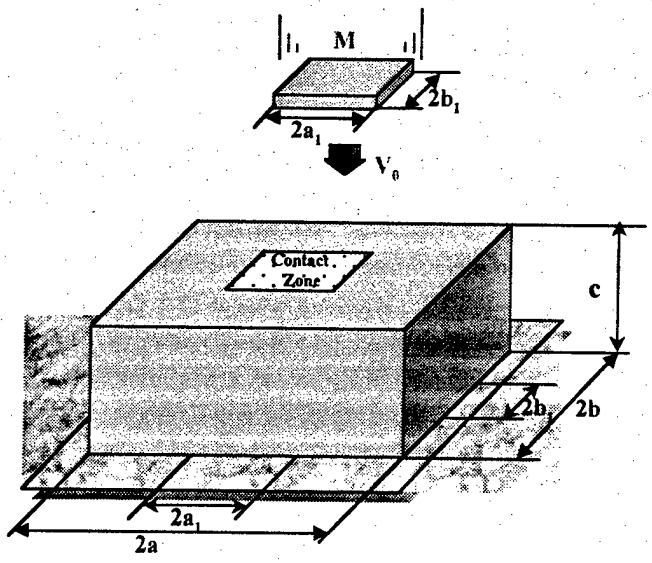

Fig.2.16. Schematic of the transverse impact loading with assumed contact zone.

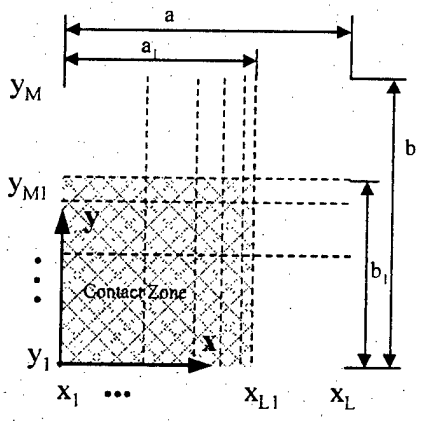

Fig.2.17. Schematic of the brick mesh covering $1/4^{th}$ of the contact zone.

The symmetry properties of the problem are utilized again. Origin of the coordinate system is placed in the center of the bottom surface, so the analyzed plate region is reduced to 1/4 of its full size and is defined as

$0 \le x \le a,\ 0 \le y \le b,\ 0 \le z \le c$

A nonuniform brick mesh is taken within the contact zone; the mesh is specified as following (see Fig. 2.16):

$$\frac{x_{I+1}}{x_I} = 0.3 \text{ for } I = 1,\ldots,L_1\text{-}1,\ L=L_1+1 \qquad (2.21)$$

$\frac{y_{j+1}}{y_j} = 0.3$ for j = 1,...,M_1-1, M=M_1+1

Calculations were carried out for L_1 = 3, 4, 5 and M_1=3. A single brick in the z-direction was used in this example. Results of the numerical simulation are presented in Figures 2.18 – 2.21.

Distributions of the transverse displacement and strain along the x-coordinate are shown in Fig. 2.18. Over the contact area, the longitudinal displacement is uniform and is equal to the projectile displacement, while distribution of the strain is highly nonuniform. The maximum compressive strain is reached at the end of the contact zone. The minimum value of the compressive strain is observed at the center of the contact zone. Time variations of the transverse strain at the points x=0 and x=a_1 are shown in Fig. 2.18. When comparing results presented in Figs. 2.18 and 2.19 for different meshes (those corresponding to L+ = 3, 4, 5) within the contact zone, one can conclude that the converged solution has been obtained for the displacement and strains. The solution convergence for the contact pressure is illustrated for two locations inside the contact zone in Figs. 2.20 a,b. At the same time, as seen from results presented in Fig. 2.20c, magnitude of the contact pressure near the end of the contact zone is highly sensitive to the mesh refinement. Also, it is seen that the contact pressure exactly at the end of the contact zone is about three orders of magnitude higher than that inside the contact zone but at small distance from the end of the contact zone. It is anticipated that with further mesh refinement this value will further grow. This means that the stresses at the end of the contact zone may be singular. Further results shown in Fig. 2.21 illustrate that the mesh refinement near the end of the contact zone results in significant increase of the contact pressure. The anticipated singularity of contact pressure at the end of the contact zone is, certainly, related to the assumed prismatic shape of the projectile.

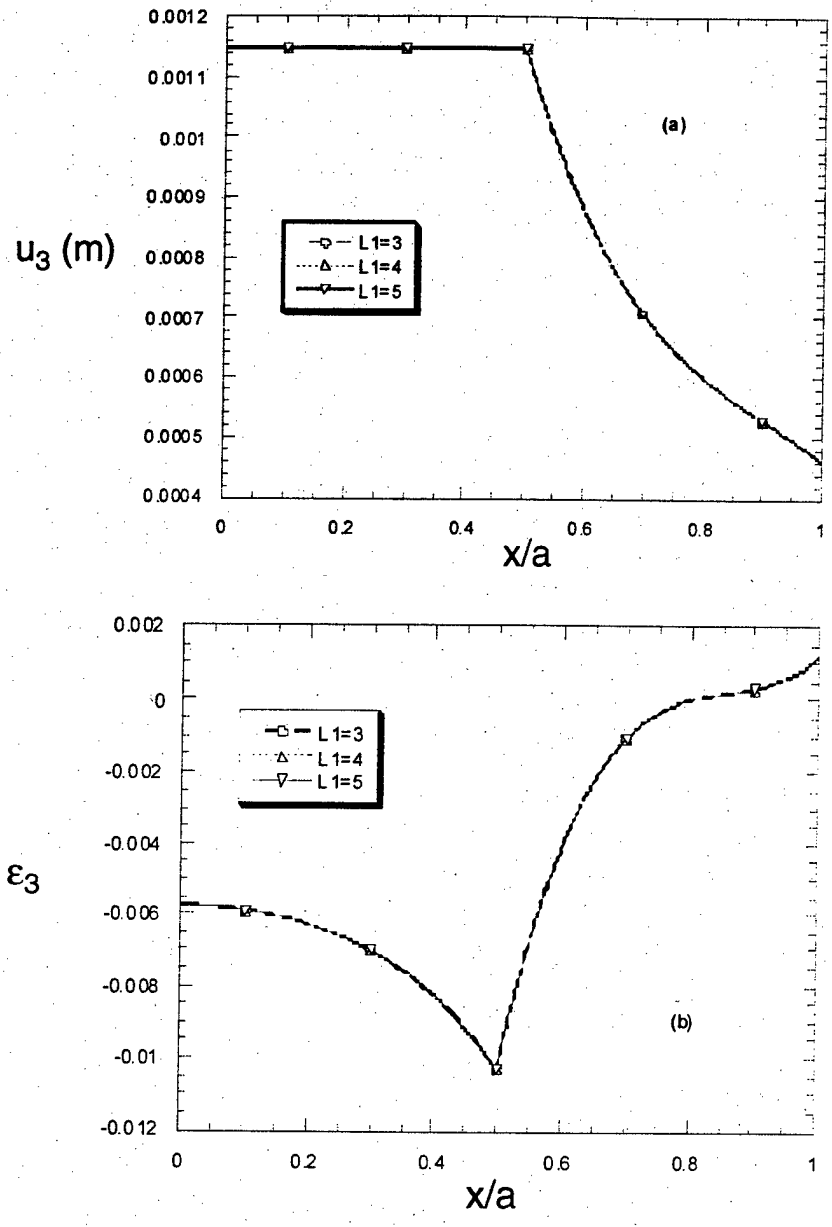

Fig.2.18. Distributions of the transverse displacement (a) and strain (b) along the x-coordinate at time instant τ=4; y-0, z=c.

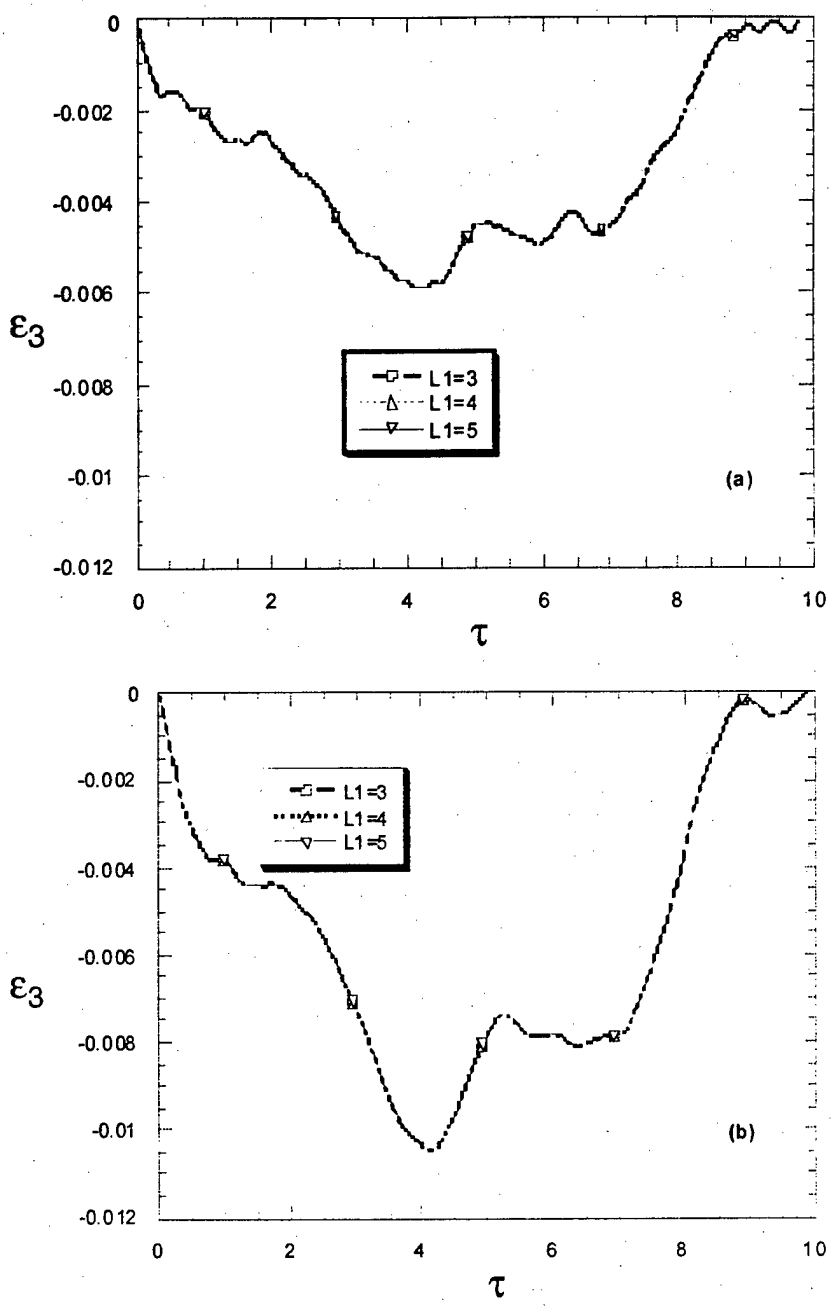

Fig.2.19. Time variations of the longitudinal strain ε_3 at x=0 (a) and at x=a/2 (b); y=0, z=c.

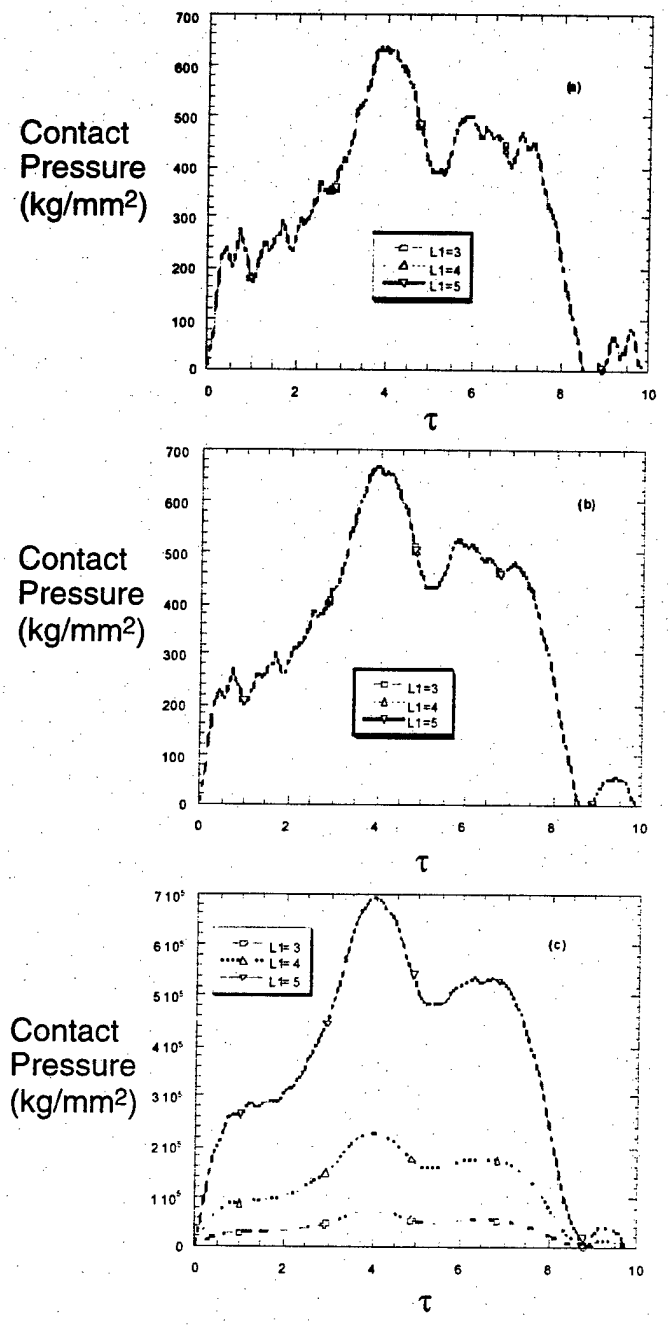

Fig.2.20. Time variations of the contact pressure at x=0 (a), x=a_1/2 (b) and at x=a (c); y=0, z=c.

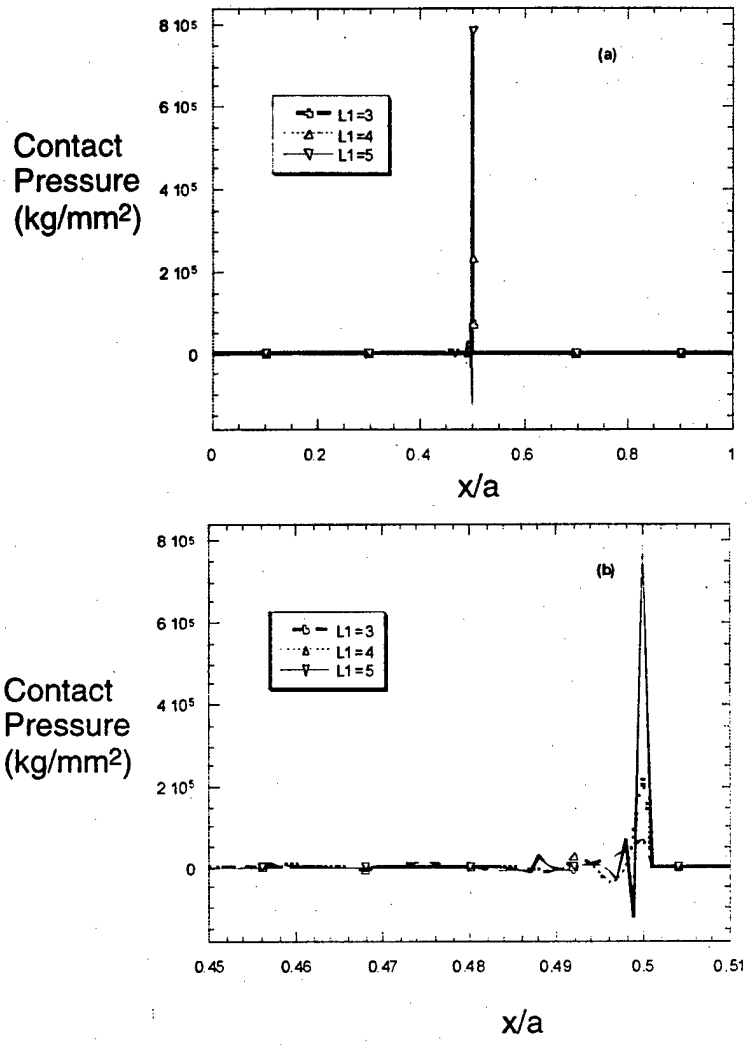

Fig.2.21. Distributions of the contact pressure in the x-direction at y=0, τ=4 for various numbers of bricks within the contact zone.

2.4. Impact Contact Analysis of Textile and Laminated Composite Plates

Transverse impact loading problem with assumed contact zone, as described in the Section 2.3 and schematically shown in Fig. 2.15, is further studied here for textile and laminated composite plates.

The textile material is 3D woven composite with orthogonal reinforcement architecture

[5] as shown in Fig. 2.22. Specifications of the 3D orthogonal woven composite material are given in Table 2.2. Elastic constants of the 3D orthogonal woven composite are:

$$E_x = 53.7GPa,\ E_y = 65.1GPa,\ E_z = 16.6GPa$$

$$G_{yz} = 4.09GPa,\ G_{xz} = 3.90GPa,\ G_{xy} = 4.74GPa \qquad (2.22)$$

$$\nu_{xy} = 0.056,\ \nu_{xz} = 0.32,\ \nu_{yz} = 0.31$$

Density of the composite is $1500kg/m^3$.

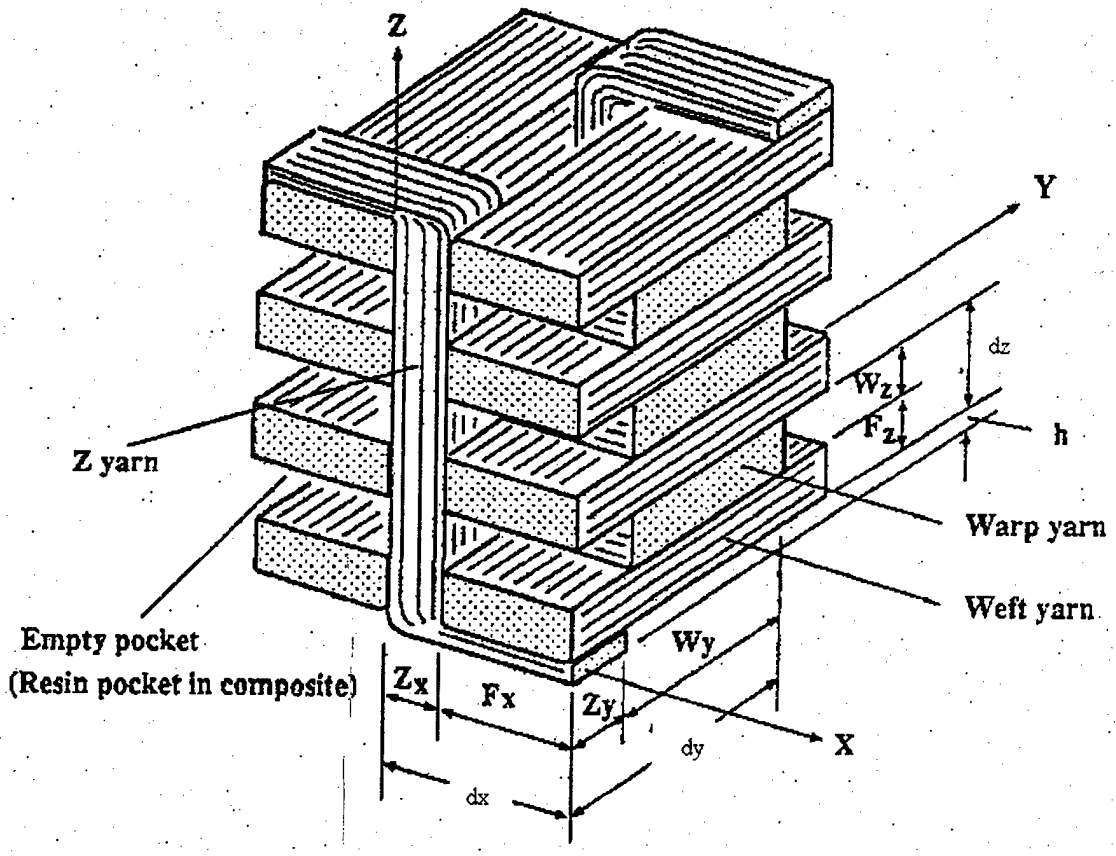

Figure 2.22. The structure of 3D orthogonal woven fabric.

Table 2.2. Specifications of the 3D Orthogonal Woven Material

Material of the fabric: Celion® G30-500 carbon fibers;
Size of yarns: warp yarn: 12K, 5 layers;
filling yarn: 2←6K, 6 layers;
Z yarn: 3K;
Reed density = 5.51 *dents / cm* (14*dents / in.*)
Pick density = 5.51 *picks / cm* (14*picks / in.*)
Preform thickness = 5.4 *mm*
Matrix: Tactix 123 epoxy resin

The laminated composite plate of [0/90/0] lay-up is made from plies of unidirectional Graphite/Epoxy tape AS4/3501-6. Thickness of the 90^0 ply is twice of the thickness of 0^0 plies. The following elastic characteristics have been adopted in the analysis:

$$E_L = 133GPa,\ E_T = 10.7GPa,\ G_L = 7.03GPa,\ G_T = 4.07GPa,\ \nu_{LT} = 0.30 \tag{2.23}$$

The density of the laminated composite is $1580kg/m^3$.

Simulations were carried out for rectangular plates made from the above 3D woven and laminated composites. Dimensions of the plate and size of the contact zone are prescribed as a=b=70mm, a_1=b_1=5 mm, c=5.4mm (see Fig. 2.15 for notations). Numerical results have been obtained for the third degree Bernstein basis functions used for the three coordinate directions. Number of bricks used to simulate contact problem for the woven composite plate was taken 3x3x2, and for laminated composite plate 3x3x3. The brick mesh parameters are defined as follows

$L_1 = 2$, L=3, M_1=2, M=3, N=2

$$x_1/x_2 = 5,\ x_2 = a_1,\ x_3 = a;\ y_1/y_2 = 5,\ y_2 = b_1,\ y_3 = b;\ z_1/z_2 = 10,\ z_2 = c \tag{2.24}$$

for the woven composite plate and

$$L1 = 2,\ L = 3;\ M1 = 2,\ M = 3;\ N = 3;$$

$$x_1/x_2 = 5,\ x_2 = a_1,\ x_3 = a;\ y_1/y_2 = 5,\ y_2 = b_1,\ y_3 = b;\ z_1 = c/4,\ z_2 = 3c/4,\ z_3 = c \tag{2.25}$$

for the [0/90/0] composite plate.

Simulation results for the projectile mass $M = 64.4g$ and projectile velocity $V_0 = 1.41m/s$ are shown in Figs. 2.23 - 2.26. Figs. 2.23 and 2.24 show variations of the projectile

displacement and velocity in time for the 3D woven and laminated plates. It is seen that displacement of the projectile increases monotonically from zero to its maximum value, and at the some time instant, velocity of the projectile decreases to zero. At the upward phase of the projectile movement, the displacement of the projectile decreases while velocity of the projectile increases to almost its initial value. Then, at certain time instant, the contact between the projectile and plate is lost.

Variations in time of the contact pressure, the transverse normal stress σ_{33}, and longitudinal normal stress σ_{11} at the center of the plate top surface (x=y=0, z=c) are shown in Figs. 2.25 and 2.26. The stress component σ_{33} shown in Fig. 2.26 is re-plotted with opposite sign and shown in Fig. 2.25 by dotted line. It is seen that the difference between the computed contact pressure and the stress value $(-\sigma_{33})$ is barely visible. Therefore, the imposed non-penetration condition (see, equation (2.1) of [2]) is satisfied with high accuracy in the obtained solution. This remarkable result is, certainly, nontrivial, since the contact pressure is calculated directly by the use of Lagrangian multiplier functions, while the normal stress at the surface of the plate are are calculated from totally different equations (namely, from the stress-strain relations of 3D elasticity).

Figs. 2.23 - 2.26 allow one to compare impact response of 3D woven and laminated plates. First observation following from Fig. 2.23a and Fig. 2.23b is that maximum displacement of the projectile is higher in the case of laminated composite plate. This result is explained by the fact that stiffness in the *z*-direction of the laminated plate is lower than that of the woven plate. The same higher *z*-direction stiffness of the woven target also results in a higher peak contact pressure compared to the peak contact pressure for the laminated plate, as seen in Figs. 2.25a and 2.26b.

Another interesting observation, following from Figs. 2.24 and 2.25, is that the contact time is lower for the woven composite plate. This is related to the shorter time required for the transverse stress wave to propagate through the thickness of the woven plate.

This time is $\tau_1^* = 1.57\mu s$, as compared to $\tau_2^* = 1.97\mu s$ for the laminated plate.

Finally, the higher stiffness in the *x*-direction for the laminated plate results in a higher peak value of σ_{11} for the laminated plate as compared to the peak value of σ_{11} for the

woven plate, as seen in Fig. 2.26.

Figs. 2.27 and 2.28 show variations of the contact pressure for the 3D woven and laminated composite plates. Simulations were carried out at three different combinations of the projectile velocity and mass. The projectile kinetic energy is kept the same for all three cases. It is seen that the shape of the contact pressure distribution changes when the projectile velocity increases. Also, two important conclusions can be drawn from Figs. 2.27 and 2.28. First, the contact time decreases as the projectile velocity increases. Second, the peak of contact pressure increases as the projectile velocity increases. Both these conclusions are consistent with the available experimental observations.

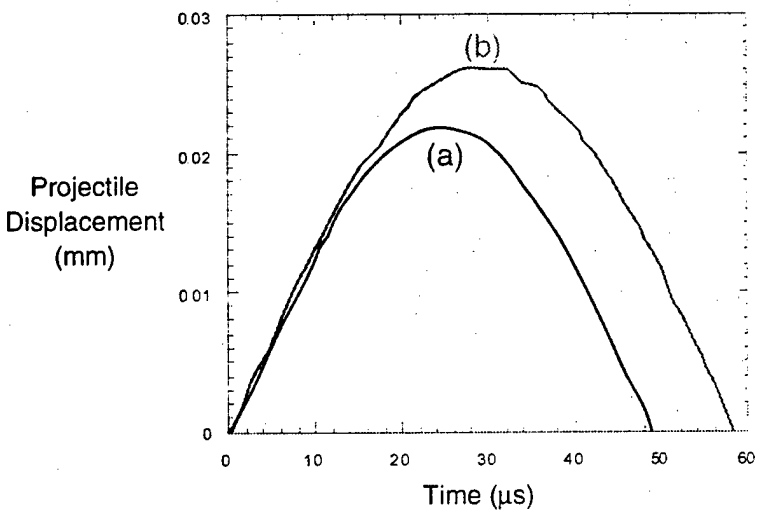

Figure 2.23. Variations of the projectile displacement in time for impact loading of 3D woven (a) and [0°/90°/0°] laminated (b) composite plates.

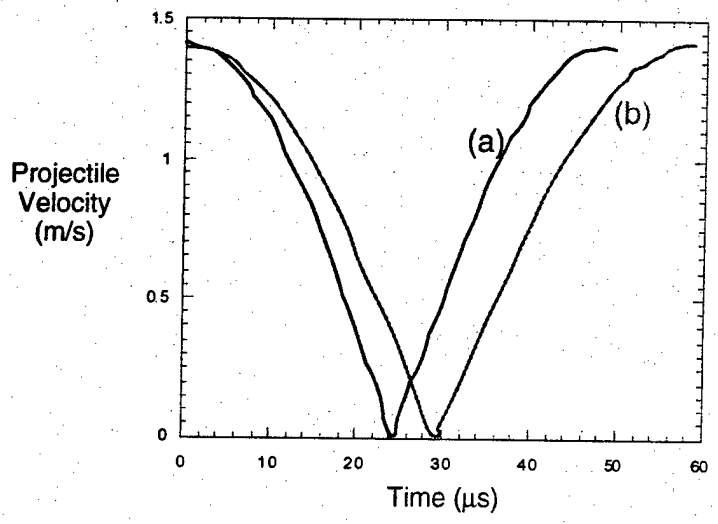

Figure 2.24. Variations of the projectile velocity in time for impact loading of 3D woven (a) and [0/90/0] laminated (b) composite plates.

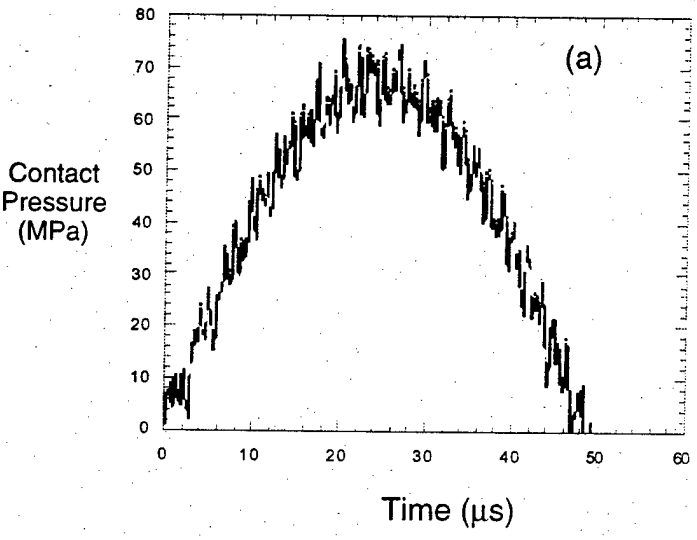

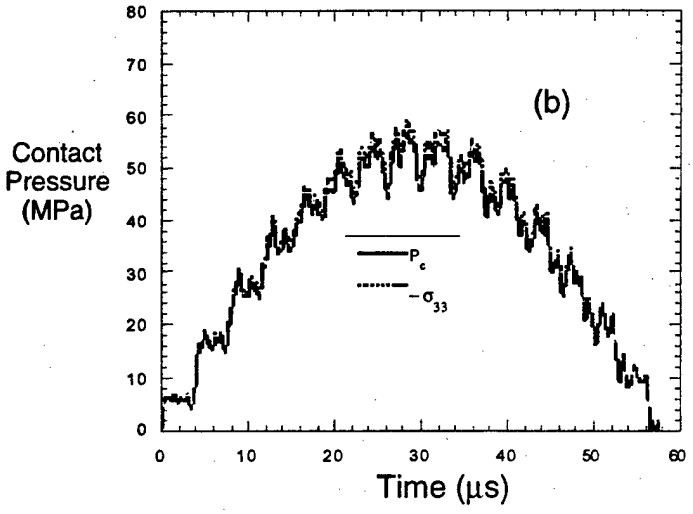

Figure 2.25. Variations of the contact pressure (solid lines) in time for impact loading of 3D woven (a) and [0/90/0] laminated (b) composite plates. Dashed lines show variation of the stress component ($-\sigma_{33}$) in the plate calculated at $x = y = 0$, $z = c$.

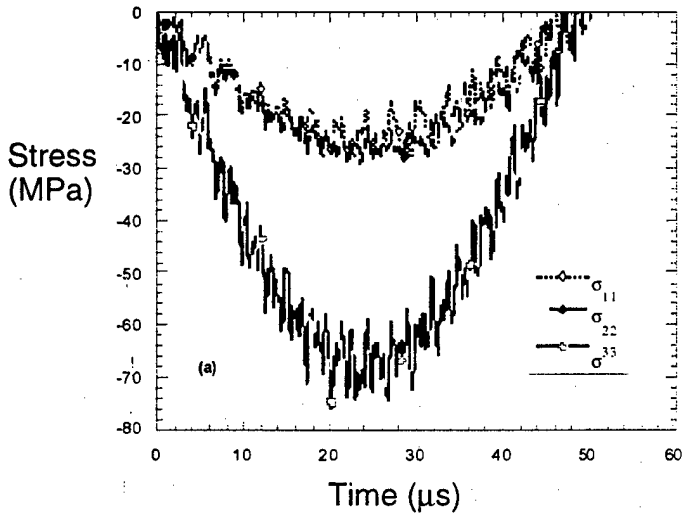

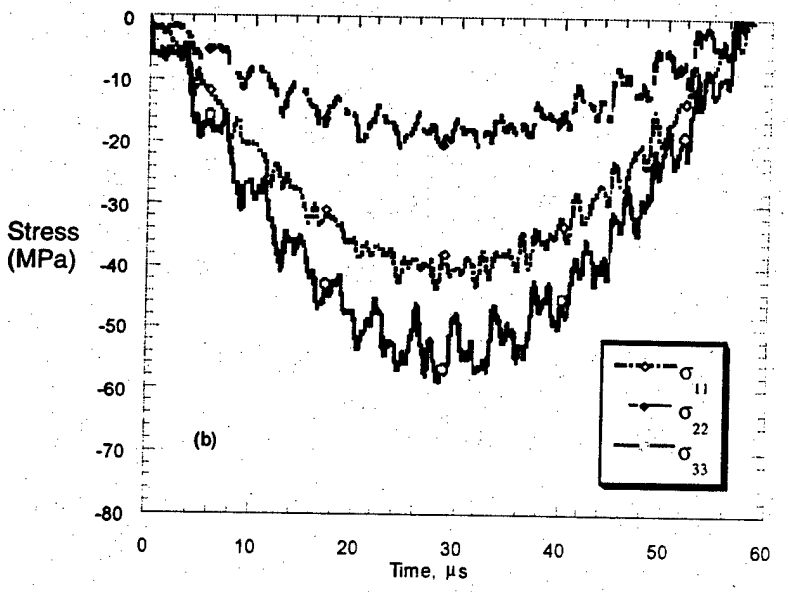

Figure 2.26. Variations of the stress components σ_{11}, σ_{22}, and σ_{33} in time for 3D woven (a) and [0/90/0] laminated (b) composite plates. Stresses are calculated at x=y=0, z=c.

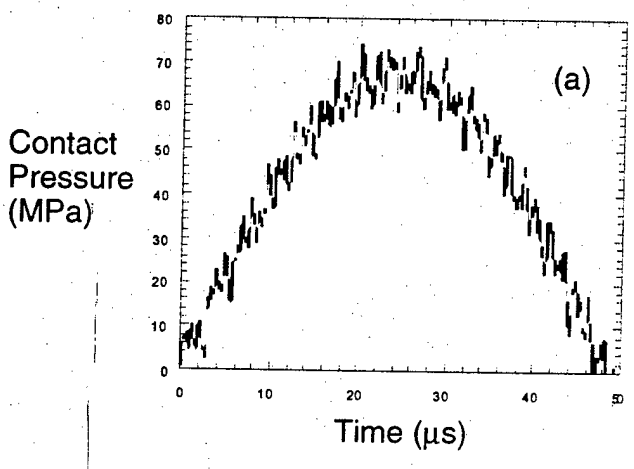

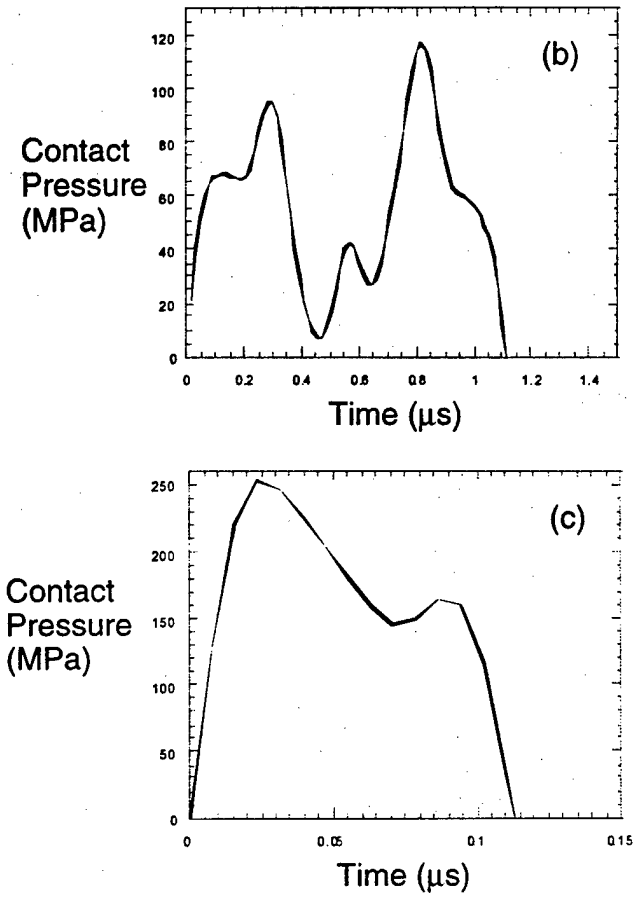

Figure 2.27. Variations of contact pressure in time for the 3D woven composite plate; $V_0 = 1.41 m/s$, M=64.4g (a); $V_0 = 14.1 m/s$, M=0.644g (b); $V_0 = 70.5 m/s$, M=0.2576g (c).

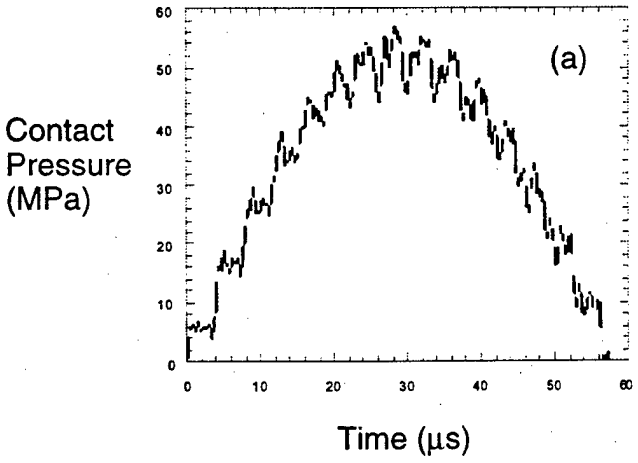

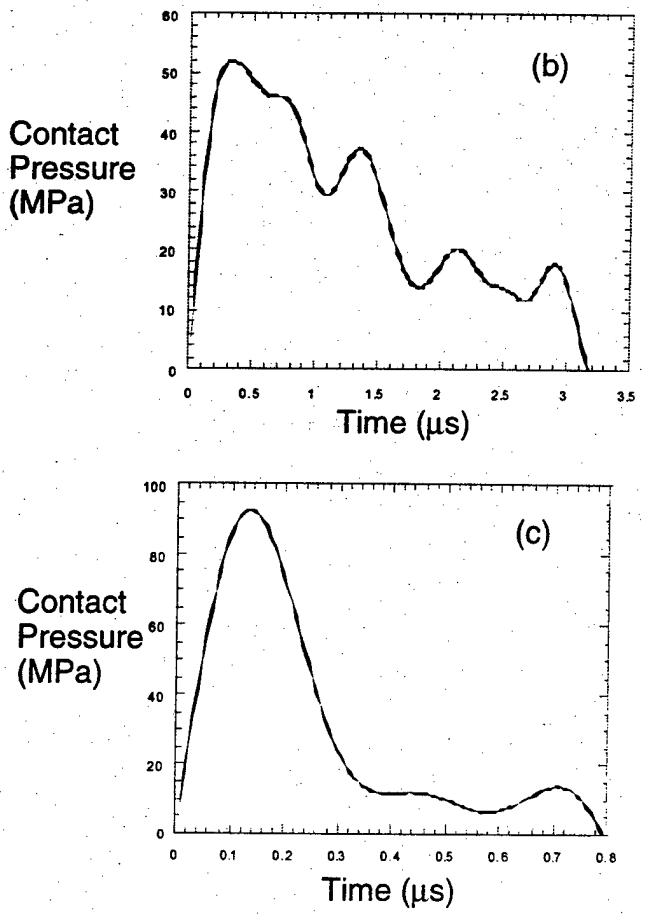

Figure 2.28. Variations of contact pressure in time for the laminated composite plate; $V_0 = 1.41 m/s$, M=64.4g (a); $V_0 = 14.1 m/s$, M=0.644g (b); $V_0 = 70.5 m/s$, M=0.2576g (c).

3. Tensile Response of 3D woven fabrics

The tensile mechanical response of woven fabrics has been studied by a number of investigators. Most researchers point to the classical work of Peirce (1937) and the modifications by Love (1954), Kemp (1958), and Abbot et al. (1973) as the critical starting point in this field. Whereas Peirce approached the modelling of woven fabric tensile response from a geometry-force approach, there have been a variety of methods applied since. The published models used to analyze and predict the tensile properties of woven fabrics include geometrical, mechanistic, energy and statistical models.

Most of the research on the tensile properties of woven fabrics has studied plain weaves. Work has been performed in this area by many researchers including Kilby (1963), Olofsson (1964), Grosberg and Kedia (1966), Kawabata et al. (1973, 1973a), Postle and De Jong (1977), Sharkas and Leaf (1987), Anandjiwala and Leaf (1991, 1991a) and Sun et al. (1997). Some work specific to twill weaves has been performed by researchers such as Kawabata and Niwa (1979) and Williams (1990).

Only recently have generalizations accounting for more than one type of warp and filling yarns and varying weave tightness been considered. Predictive models of the load-extension properties of these complex weaves have been published by Reumann (1990), and Realff et al. (1993, 1997) amongst others.

3.1. Geometrical Modelling

The pioneering geometrical approach by Peirce (1937) remains one of the most complete works on plain weave structure and its properties. Peirce's work was more concerned with the shape and position of the yarns in the fabric structure rather than with the mechanical behavior of the fabric subjected to an applied tensile load. However, several workers have used both his rigid and his flexible thread models as starting point in their later studies. For example, Shanahan and Hearle calculated the biaxial extension of plain woven fabrics with an energy method, using Peirce's flexible thread model (**Error! Reference source not found.**) with the assumption of circular cross-section and zero bending resistance of yarns. Subsequently they developed their own 'lenticular geometry' model considering that the shape of the yarn was similar to that of a lens or a football, and can be represented by two intersecting arcs as shown in Figure

3.2.

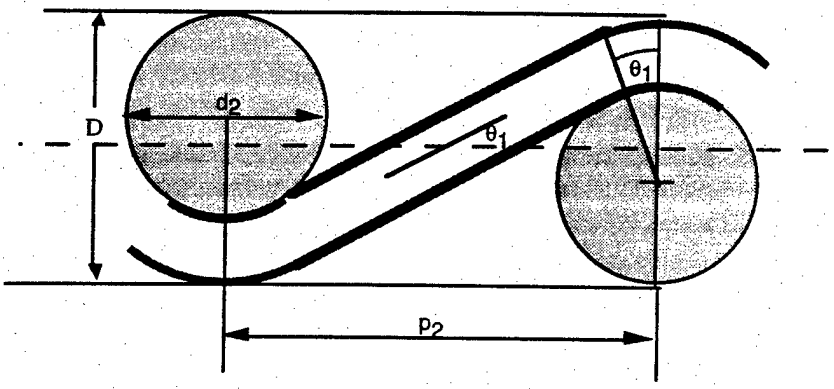

Figure 3.1 Peirce's flexible thread model.

Figure 3.2 Shanahan and Hearle's lenticular geometry.

Other researchers developed different geometries that seemed to be more suitable to represent the real shape of the yarn cross-section in a cloth. Peirce himself observed that his assumption of a circular cross-section of thread was invalid in practice, due to the thread flattening which usually occurs during the weaving process, thus he modified this assumption considering a more realistic elliptic cross-section. He concluded, however, that the formal treatment of the elliptic section would lead to complex formulae (including the solution of elliptic integrals), whose application in the

study of actual cloths would be considerably more laborious and probably no more effective than the approximate treatment of flattened threads. In his approximate treatment he used the geometrical equations that he had derived for circular threads, merely replacing the diameter of the circular thread section by the minor axis of the elliptic section. To assist in the practical determination of the cloth geometry, Peirce produced also a set of curves and tables connecting the various geometrical parameters experimentally determined.

Kemp (1958) modified Peirce's model by suggesting a 'race-track' section (a rectangle joined with semi-circles on left and right) as the shape for the yarn cross-section in the fabric. In addition to being closer to the actual shape of the yanr section than the circular section, the race-track section had an advantage over the ellipse because the formulae developed from it were similar to those given by Peirce for the circular section.

Olofsson (1964) used a 'twin-arc' model assuming that the path of the yarn consists of two arcs, one above and one below the central plane of the fabric.

Kawabata (1973) produced the so-called triangle-wave model which represents the simplest geometry for the plain weave fabric. Many recent works on the tensile behavior of woven fabrics (Realff et al (1997), Reumann (1990), Sun et al. (1997) for example) refer to Kawabata's straight lines and either the uniaxial or biaxial deformation theories.

The present work refers to Kawabata's approach (1973a) to estimate the uniaxial load-extension characteristics of a 3-D woven fabric. When considering a three dimensionally woven fabric, the geometrical model of the internal structure is different from the 'saw-tooth' model due to the multiple layers. The presented model refers also to Peirce's flexible thread model and to the jammed conditions defined by Peirce because of their better approximation of the yarn conditions in the 3-D woven fabric.

3.2. Peirce's Geometrical Model

Peirce [12] showed that, if it is assumed that the bending resistance of the yarns is negligible and that the yarn is circular in cross-section, a purely geometrical model which involves no consideration of internal forces can be set up for the determination of the various parameters of interest in a woven structure. In other words, he assumed that the geometry was not the result of the balance of various internal forces since no forces were needed to produce the geometry postulated. Since the yarn bending resistance is negligible, the yarn can be considered straight at all points except where it is wrapped around the crossing threads, when it is circular in shape as shown in Fig. 3.3.

Using the following symbols to designate the geometrical parameters of the fabric

P: Thread spacing; the distance between two planes, normal to the fabric, containing two successive cross yarns

l: Modular length; length of thread axis between planes containing the axes of consecutive cross threads

c: Yarn crimp, defined as the fractional excess of the yarn length over the length it covers in the cloth, $(l\text{-}p)/p$

d: Yarn diameter

h: Modular height; maximum displacement of the thread axis, normal to the plane of the cloth

θ: Weave angle; the maximum angle of the thread axis with the fabric central

plane.

D : Scale factor; sum of warp and weft diameters

and considering the subscript '1' for referring to the warp parameters, and '2' for the weft parameters, Peirce's geometry leads to the following relationships between the observable quantities of the cloth structure:

$$p_2 = (l_1 - D\theta_1)\cos\theta_1 + D\sin\theta_1 \tag{3.1}$$

$$h_1 = (l_1 - D\theta_1)\sin\theta_1 + D(1 - \cos\theta_1) \tag{3.2}$$

$$c_1 = \frac{l_1}{p_2} - 1 \tag{3.3}$$

$$h_1 + h_2 = d_1 + d_2 = D \tag{3.4}$$

Another set of equations corresponding to equations (3.1), (3.2) and (3.3) can be derived for the weft direction, so that at the end a total of seven equations connecting the eleven geometrical parameters is available, and therefore if any four of these parameters are known, such as thread spacings and crimps, the others can be calculated.

As already mentioned, because of the difficulties involved in solving these simultaneous equations for any set of unknowns, Peirce and more recently Love have produced a set of curves and nomographs to help in the calculation. Moreover, for practical uses, Peirce derived some simple approximate relationships, the most important of which is:

$$h_1 = \frac{4}{3} p_2 \sqrt{c_1} \tag{3.5}$$

that reproduces the rigorous values well enough for many purposes; only in extreme structures Peirce showed that the error amounted to 5%.

In considering jamming conditions, Peirce simplified the previous rigorous equations (3.1) and (3.2) noting that for the closest weave condition $\frac{l_1}{D} = \theta_1$ and thus

$$\frac{p_2}{D} = \sin\frac{l_1}{D} = \sin\frac{(1+c_1)p_2}{D} \tag{3.6}$$

and

$$\frac{h_1}{D} = 1 - \cos\frac{l_1}{D} \tag{3.7}$$

3.3. Kawabata's Uniaxial Deformation Theory

Kawabata's 'saw-tooth' geometry [5, 6] is the simplest structural model of a plain weave fabric; it assumes in fact that the warp and weft yarns are straight lines which bend at the crossing points (see **Figure 3.3**). With this simplification, the structural constants necessary for the deformation theory derive from the four original structural constants:

n_1 = warp yarn density in the undeformed state (ends/cm)

n_2 = weft yarn density in the undeformed state (picks/cm)

S_1 = warp yarn crimp caused by weaving which is defined by $(l_{01} - y_{01})/y_{01}$,

where l_{01} is the length of the warp yarn in the unit structure and y_{01} is the filling thread spacing in the undeformed state

S_2 = weft yarn crimp caused by weaving which is defined by $(l_{02} - y_{02})/y_{02}$,

where l_{01} is the length of the weft yarn in the unit structure and y_{02} is the warp thread spacing in the undeformed state

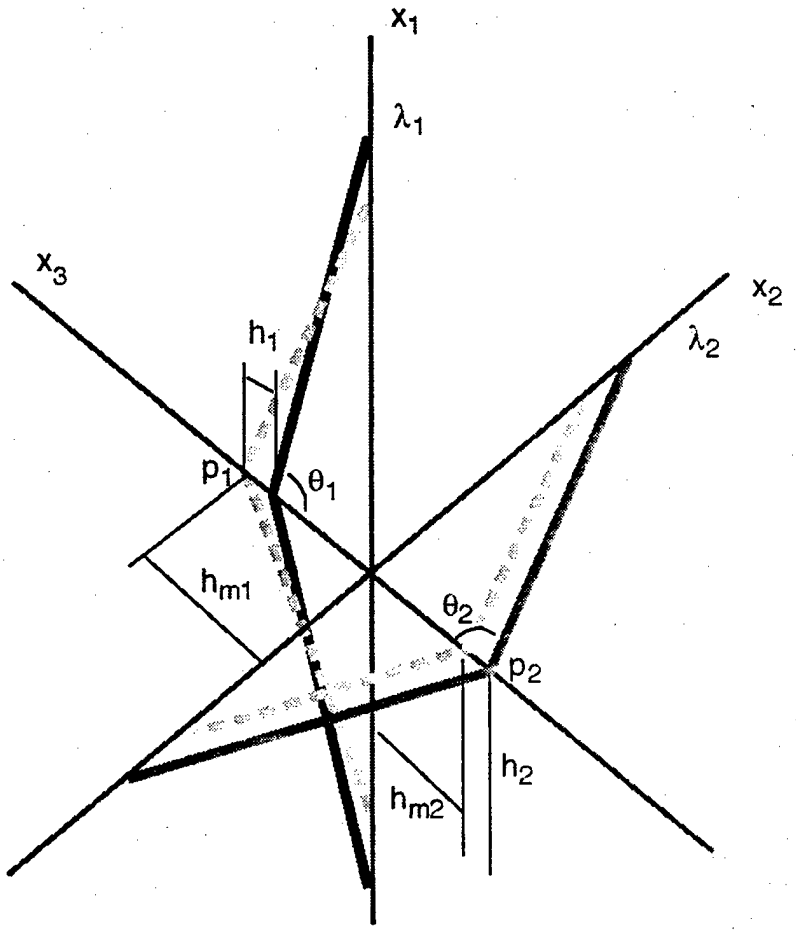

Figure 3.3 Kawabata's unit cell geometry of a plain weave fabric.

The structural constants derived from the above are as follows:

$$y_{01} = \frac{1}{n_2} \quad \text{(i)}, \qquad y_{02} = \frac{1}{n_1} \quad \text{(ii)}$$

$$\sin\theta_{01} = \frac{1}{S_1 + 1} \quad \text{(iii)}, \qquad \sin\theta_{02} = \frac{1}{S_2 + 1} \quad \text{(iv)}$$

$$l_{01} = \frac{y_{01}}{\sin\theta_{01}} \quad \text{(v)}, \qquad l_{02} = \frac{y_{02}}{\sin\theta_{02}} \quad \text{(vi)}$$

$$h_{m1} = \frac{l_{01}}{2}\cos\theta_{01} \quad \text{(vii)}, \qquad h_{m2} = \frac{l_{02}}{2}\cos\theta_{02} \quad \text{(viii)}$$

where y = thread spacing

θ = the angle between the yarn axis and the X_3- axis in the structural model

l = the yarn length in the unit structure

h = the deflection of the point at which the yarn axis intersects the X_3- axis. The deflection is caused by the stretch ratios λ_1 and λ_2 of the fabric; that is, h_1 is the movement of point p_1 and h_2 that of p_2 in Fig. 11.

h_m = the distance between the neutral line and the yarn axis along the X_3- axis in the undeformed state; this is also equal to the maximum value of h

Kawabata uses the structural model presented above to solve the problem of uniaxial deformation. For the direction in which the stress is applied, he assumes the yarns to be perfectly flexible and introduces the effect of bending on the transverse yarn, which was instead neglected in the case of biaxial deformation.

When a tensile force is applied in warp direction, the yarns along the same direction tend to straighten while the yarns in the transverse direction, the filling yarns, bend because no tension is applied along their direction. Thus the force F_c caused by the tension on the warp yarns is equal to the force required to bend the filling yarns.

For the equilibrium of the forces acting in the deformed state along the X_3-axis (forming a rectangular co-ordinate system with the axis along the neutral lines in warp and weft directions) the following relation is derived:

$$F_c = 2F_{T1}\cos\theta_1 \tag{3.8}$$

where F_c = compressive force acting along the X_3-axis at the point of contact of the warp and the weft threads, FT1 = tension on warp yarn

Considering the relation obtained from the structural model in the deformed state

$$\cos\theta_1 = \frac{2(h_{m1} - h_1)}{\sqrt{4(h_{m1} - h_1)^2 + (\lambda_1 y_{01})^2}} \tag{3.9}$$

and representing the tensile properties of the warp yarns with a function of their stretch ratio λ_{y1} obtainable from a stress-strain test,

$$F_{T1} = g_1(\lambda_{y1}) \tag{3.10}$$

the equilibrium relation becomes

$$F_c = 2g_1(\lambda_{y1})\frac{2(h_{m1}-h_1)}{\sqrt{4(h_{m1}-h_1)^2+(\lambda_1 y_{01})^2}} \tag{3.11}$$

Considering a first approximation for the compressive force F_c caused by the tension F_{T1} in the warp yarn and acting at the point of contact of warp and weft yarns along the normal axis X_3,

$$F_c = C_0 + C_1 h_1 = 2F_{T1}\cos\theta_1 \tag{3.12}$$

and considering the following geometrical relations, deduced from Fig. 3.3, respectively for the deflection of the warp yarns and the stretch ratio of the fabric

$$h_1 = \frac{l_{01}}{2}\cos\theta_{01} - \frac{l_{01}\lambda_1}{2}\cos\theta_1 \tag{3.13}$$

$$\lambda_1 = \frac{l_{01}\lambda_{y1}}{y_{01}}\sin\theta_1 \tag{3.14}$$

the angle between the warp thread and the X_3- axis is determined as follows:

$$\cos\theta_1 = \frac{2C_0 + C_1 l_{01}\cos\theta_{01}}{4F_{T1} + C_1 l_{01}\lambda_{y1}} \tag{3.15}$$

and subsequently the tensile force on the fabric $F_1 = F_{T1}\sin\theta_1$ and the stretch ratio of the fabric are obtained from the following equations:

$$F_1 = g_1(\lambda_{y1})\sqrt{1-\left(\frac{2C_0 + C_1 l_{01}\cos\theta_{01}}{4g_1(\lambda_{y1}) + C_1 l_{01}\lambda_{y1}}\right)^2} \tag{3.16}$$

$$\lambda_1 = \frac{l_{01}\lambda_{y1}}{y_{01}}\sqrt{1-\left(\frac{2C_0 + C_1 l_{01}\cos\theta_{01}}{4g_1(\lambda_{y1}) + C_1 l_{01}\lambda_{y1}}\right)^2} \tag{3.17}$$

The constants C_0 and C_1 are the characteristic parameters of the fabric. They are calculated in Kawabata's work with considerations on yarn compression and bending behavior:

$$C_0 = -\Phi_{max} C_1 \tag{3.18}$$

where Φ_{max} is the average decrease in thickness of warp and weft threads and

$$C_1 = \frac{C_b}{1+2K} \tag{3.19}$$

The constants C_b and K are determined considering the bending of the yarn lying along the axis perpendicular to the direction of the applied tension as accompanied by fiber bending and local shear deformation and they are respectively defined as:

$$C_b = 2N\frac{192E_f I_f}{(2l_{02})^3} \tag{3.20}$$

where E_f = Young's modulus of a fiber, I_f = geometrical moment of inertia of a fiber, N = mean number of fibers in the yarn cross-section, and

$$K = \frac{2\mu D}{l_{02}} \tag{3.21}$$

where μ = coefficient of friction along the fiber

D = yarn diameter

A recent work by M. L. Realff, M. C. Boyce and S. Backer modifies Kawabata's approach considering the bending of the yarn in substitution of that of the fiber, thus formula (20) is modified as

$$C_b = 2\frac{192EI}{(2l_{02})^3} \tag{3.22}$$

where EI = bending rigidity of the yarn obtained from a four points bending test.

One reason for choosing the yarn bending response instead of the fiber bending is that the zero slopes at the walls and at the center of the beam match those of the yarn at the crossover points in the fabric, as shown in Fig. 3.4. The Kawabata's fabric geometry does not include any yarn curvature, while Realff and colleagues' beam model incorporates the yarn curvature into the bending portion of the yarn behavior.

Moreover, they affirm that Kawabata's model fails in predicting the response of the fabric at low strains because it overestimates the bending resistance of the yarn. This is in fact considered as the sum of the bending responses of the fibers in the yarn, parallel to each other and deflected by the same amount that the yarn deflects. But this is not true for a real yarn.

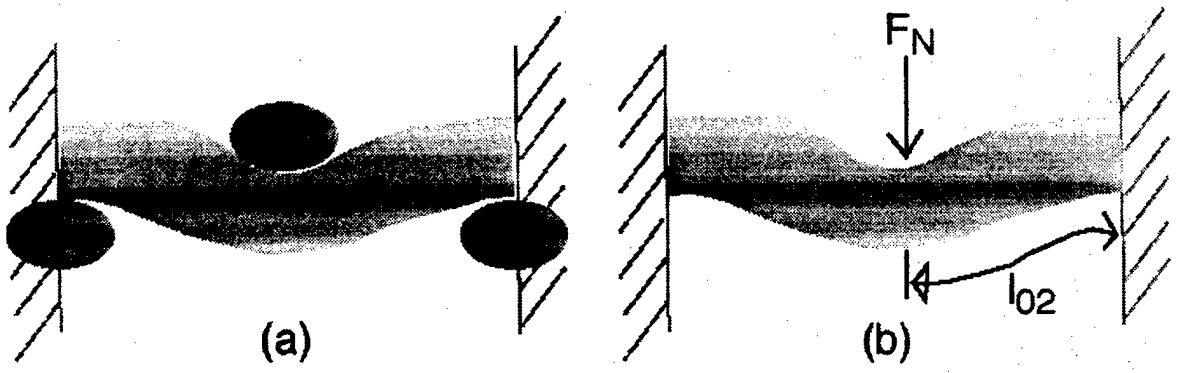

Figure 3.4 Beam theory model for the deflection of the cross yarns during fabric deformation: (a) fabric, and (b) model.

A further development introduces the concept of yarn consolidation and the tendency towards a circular cross-section due to the axial loading. The extension of the loaded yarns within the fabric is said to cause a radius reduction which leads to an increased local cross yarn curvature and to increased normal forces at the crossover points, and as ultimate consequence it causes further flattening of the cross yarn. The increase in the normal force is given by:

$$F_{Nc} = \frac{4EI}{l_{02}}\left(\frac{1}{D_{\lambda y1}} - \frac{1}{D_0}\right) \tag{3.23}$$

where $D_{\lambda y1}$ is the yarn diameter given by the consolidation experiment and D_0 is the initial diameter of the yarn.

While Realff's model is proved to predict reasonably well the fabric behavior in the low and moderate strain region, deviations from the actual fabrics response are found at higher strains. This is addressed by the researcher to the presence of strain concentrations caused by the unbending of the yarns in the loaded direction. The fibers in the higher strain regions fail first causing a small decrease in the load carrying ability of the yarns, resulting in the gradual decrease in slope of the fabric stress-strain curve.

In their work, Realff and colleagues consider only plain weaves, although with different degree of tightnes and different yarn structure, R. D. Reumann, instead, uses

Kawabata's equations for developing a basic computerized system for predicting the fabric deformation characteristics as a function of fabric weave structure, thus he considers different type of weaves.

Reumann represents a woven structure using a grid coordinate system in which the interlacing point distribution is shown as a weave pattern by the distribution of the scanning points with warp thread lifts. The calculation of the stress-strain behavior of the woven fabric is then derived from the behavior of the individual scanning points. In the case of a scanning point representing an interlacing point, Kawabata's equations for the determination of the tensile force and the stretch ratio of the fabric can be used; if a float is present, instead, Reumann considers the stress-strain behavior of the scanning point as that of the thread being used. At the site of transfer from an interlacing point to a float, fractions of both are present and a suitable account of them is taken in the calculations.

In the most recent paper by F. Sun, A. M. Seyam and B. S. Gupta, a more general model is presented, which takes in account both different weaves, as in Reumann's model, and also the variation of thread spacing with fabric tightness and different structures containing more than one kind of warp and filling yarn, as in Realff and collegues' work.

In this paper, they introduce some geometrical parameters referring to the weave structure

$a = \frac{y_f}{y_i}$ = ratio of the yarn spacing under the floats y_f and the yarn spacing at intersection y_i

N = number of threads in the weave repeat

I = number of intersections in the weave repeat

$M = \frac{N}{I}$ = weave factor

and they relate all the other geometrical constants to these parameters.

The equations used to calculate the tensile force and the stretch ratio are the same as the ones introduced by Kawabata (equations (11) and (12)), but with Reumann's

modification of deriving the total load-extension behavior of the fabric from the combination of the basic unit structures in the weave.

3.4. Modeling a Novel 3-D Fabric

The mathematical model which is proposed in this thesis for predicting the tensile behavior of a 3-D fabric derives from Kawabata's uniaxial deformation theory for plain weaves.

The theoretical work of creating the prediction model consisted into two parts. In the first part, the structure of the baseline nylon 6 fabric in three dimensions was examined and the geometrical parameters were measured. On the basis of the geometrical analysis of the original fabric and referring to the saw-tooth geometry of Kawabata's model, a new geometrical model was created.

The second part of the theoretical work was concerned with relating the fabric and the yarn mechanical properties under tensile load using mathematical functions. Kawabata's uniaxial deformation theory for a plain weave was then modified for considering the presence of stuffer yarns sandwiched between the two plain weave layers.

3.5. The Characteristics of the Geometrical Model

The geometrical model considered in the present research is derived, as already mentioned, from Kawabata's unit structure for a plain weave. Both warp and weft yarns are assumed to be perfectly flexible and compressible and they are assumed as straight lines as in Kawabata's model.

Two different models are considered for the grounds and the binders, both of them comprising the stuffer ends between two layers of fabric.

Fig. 15 and Fig. 16 represent schematic diagrams of the sections in warp (X_1-axis) and weft (X_2-axis) direction of the weaves used for grounds and binders during the first approach to the problem of determining the geometrical structure that better approximated the real structure of the 3-D fabric. It can be seen that in the sections in

warp direction different filling yarns are considered centered on the same neutral line. Similarly from the sections in filling direction, two consecutive warps or binders in the same layer are considered centered on the same neutral line. Referring to the symbols used in the figures and to the same notation used in Kawabata's geometrical model, the following geometrical relationships can be deduced:

Grounds Model

Warp direction

$$\tan \theta_{01,gr} = \frac{y_{01}}{d_f + d_{gr}} \tag{24}$$

Filling direction

$$\tan \theta_{02,gr} = \frac{y_{02}}{d_f + d_{gr}} \tag{25}$$

or

$$\tan \theta_{02,gr} = \frac{y_{02}}{d_f + d_{gr}/2 + d_{bi}/2} \tag{26}$$

Binders Model

Warp direction

$$\tan \theta_{01,bi} = \frac{y_{01}}{2d_f + D_{stf} + d_{bi}} \tag{27}$$

Filling direction

$$\tan \theta_{02,bi} = \frac{y_{02}}{d_f + d_{gr}/2 + d_{bi}/2} \tag{28}$$

where y_{01} = average thread space in warp direction in the undeformed state

y_{02} = average thread space in filling direction in the undeformed state

d_f = diameter of filling yarn

d_{gr} = diameter of ground yarn

d_{bi} = diameter of binder yarn

D_{stf} = height of the unit cell occupied by the stuffer yarns, approximated with a rectangle in both warp and weft direction

In the ground model, in the filling direction, two different equations are used. The repeat unit in the original fabric was supposed to consist of a sequence of two grounds followed by a binder thread; the filling yarn therefore forms two different angles when interlacing with a ground or with a binder. This fact should be considered when the ground and binder ends are of different sizes and subsequently two different tensile models considering the two different angles formed by the filling yarn should be considered and a mean tensile response should be calculated. In the initial steps in the validation process of the tensile model, where the fabric was considered being made entirely of nylon 6 yarns, only equation 3.25 was considered in the filling direction for both the ground and the binder models and this simplified the calculations.

A more detailed analysis of the original 3-D fabric showed that the repeat unit consisting of two grounds followed by a binder thread was really only the sequence on the outer layers of the fabric and not the unit structure of an entire ground layer. The geometrical model was then modified considering the unit structure in one ground layer as formed by four grounds followed by one binder and considering the presence of a filling float due to the presence of two consecutive ends (one ground and one binder) on the same side of the filling yarn (Fig. 3.5). For the tensile response of the grounds in this new configuration an average should be calculated considering three times the force calculated for repeat 1 in the scheme and once the average force due to configuration 2 and 3. Similarly, in the binder model, the tensile response should be calculated as the average of repeats 2 and 3.

Also this second geometrical model was not completely satisfying. The jamming condition of the ground and binder ends on the outer layers of the nylon 6 fabric, the fact that no filling yarns appeared on the fabric surface, and the analysis of the encapsulated sample from which the filling yarns appeared to be almost straight, brought to the development of a third geometry. In this last geometry the structure in

warp direction was still the one in the previous models with the fillings on the same layer centered on the same line. The section in filling direction was instead modified considering no crimp of the filling yarns. This final geometrical configuration, beside being more close to the real structure of the original fabric, permitted to avoid the contradictory assumption of two adjacent warps centered on the same neutral line simultaneously with two filling yarns centered on the same neutral line. That assumption was very practical giving simple relationships defining the angles at the interlacing points, with no need of considering the actual crimp of the yarns as in Kawabata's model or the modular length h, defined by Peirce as the amplitude of the crimp wave, which are both difficult to measure. But it was unrealistic because assuming two adjacent yarns centered on the same neutral line is like assuming that they are straight, they has no crimp, and it is not possible to interlace two sets of yarns keeping them simultaneously straight in both warp and weft directions. They should have some crimp in both directions or as a limit they can be straight only in one direction at a time, as assumed in the last geometrical model that can be considered an application of Kawabata's model with the assumption of zero filling yarn crimp.

This third geometrical model was chosen for predicting the tensile response of the novel 3-D structures because no crimp of the filling yarn was considered also in the new designs and because the results obtained using one or the other model were the same for all the structures considered in the research.

It was concluded that the approximation of the various structures with a geometry that considers zero crimp simultaneously in one or the other direction is valid and useful in predicting the final tensile response of fabrics when no assumption of yarn crimp or waviness can be made.

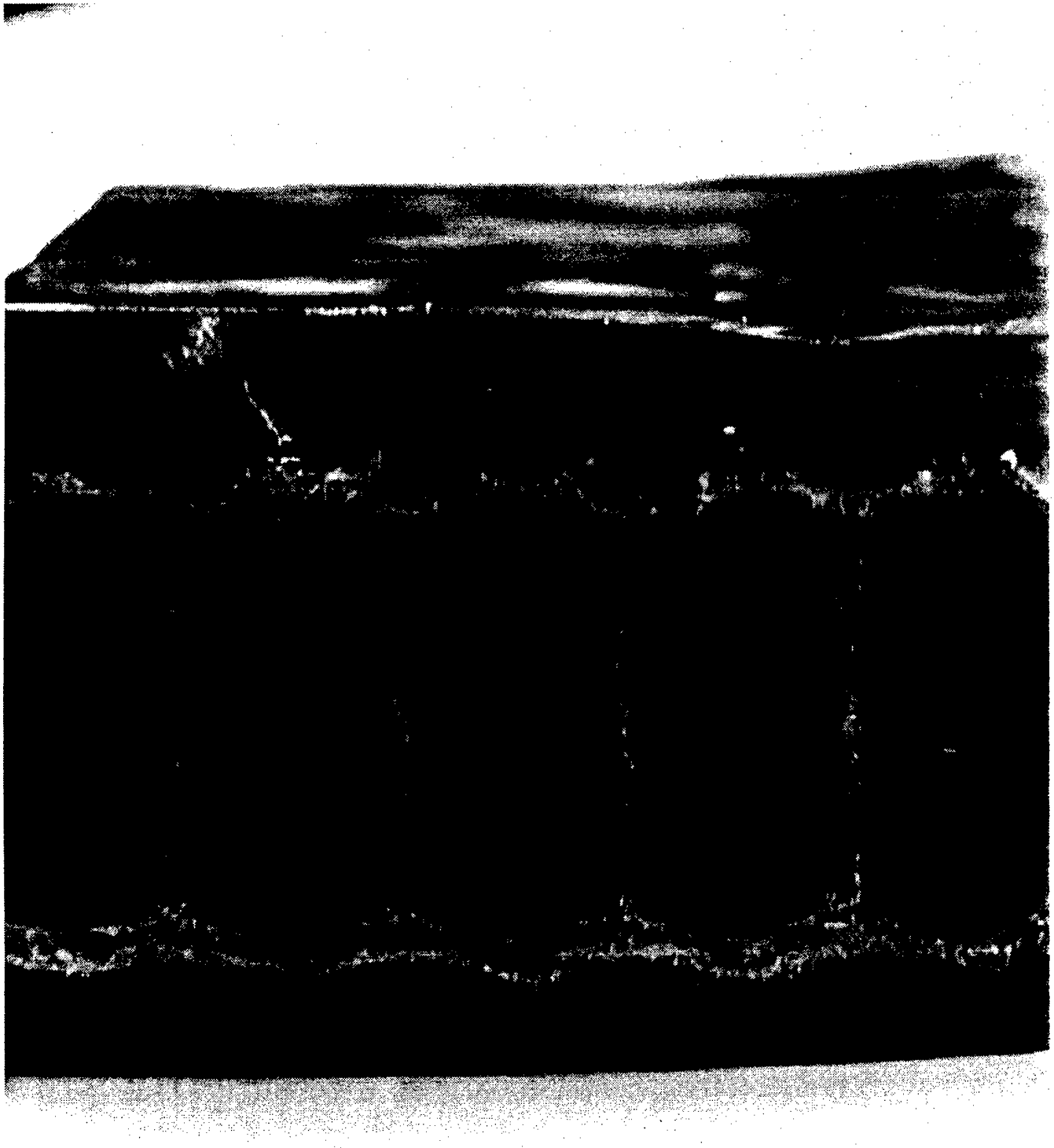

Figure 3.5 Nylon 6 baseline fabric in filling direction.

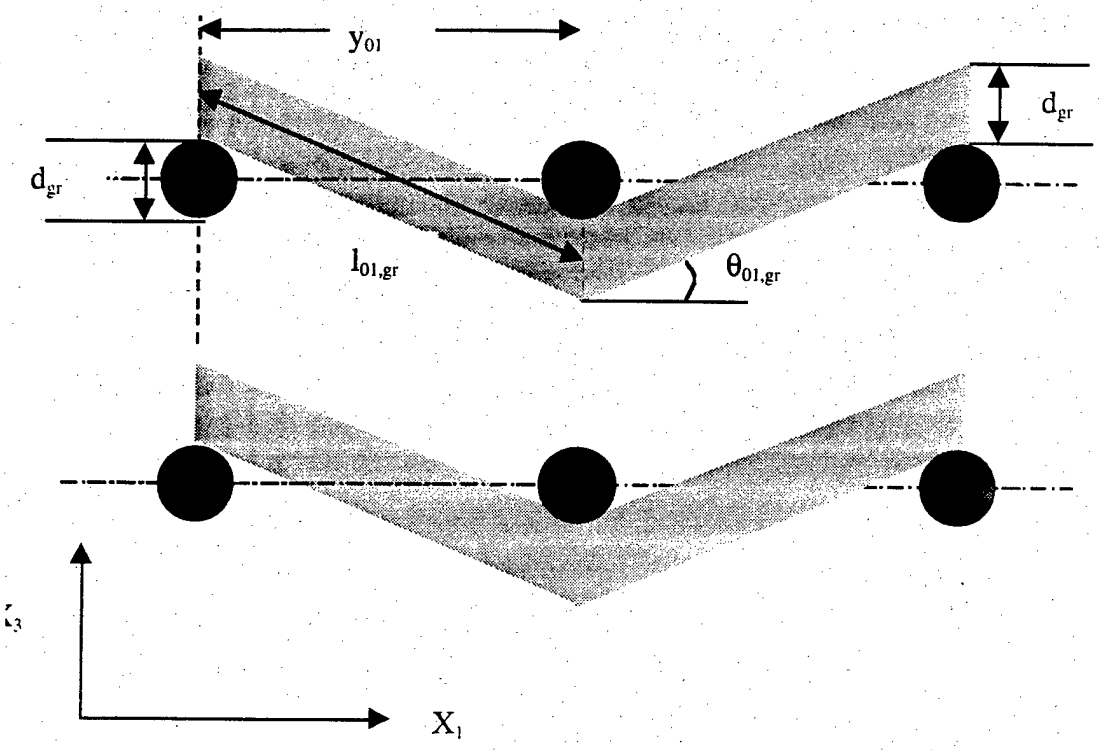

Figure 3.6 Schematic view of the baseline structure in warp direction, grounds model

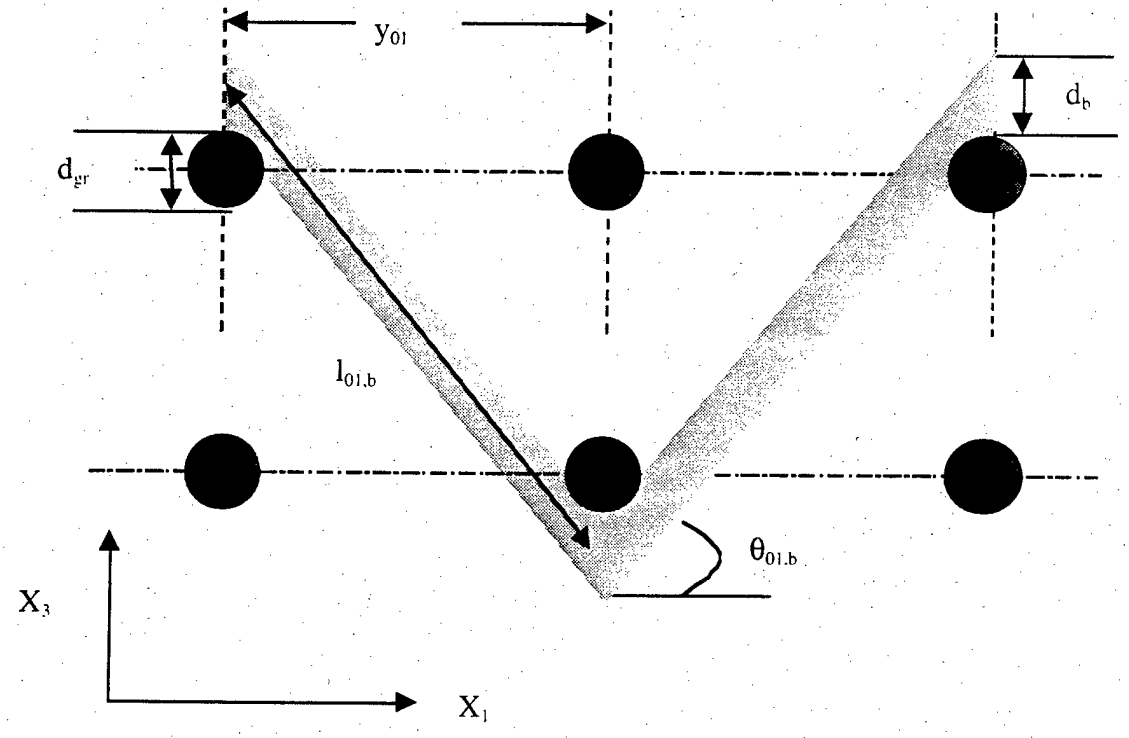

Figure 3.7 Schematic view of the baseline structure in warp direction, binders model.

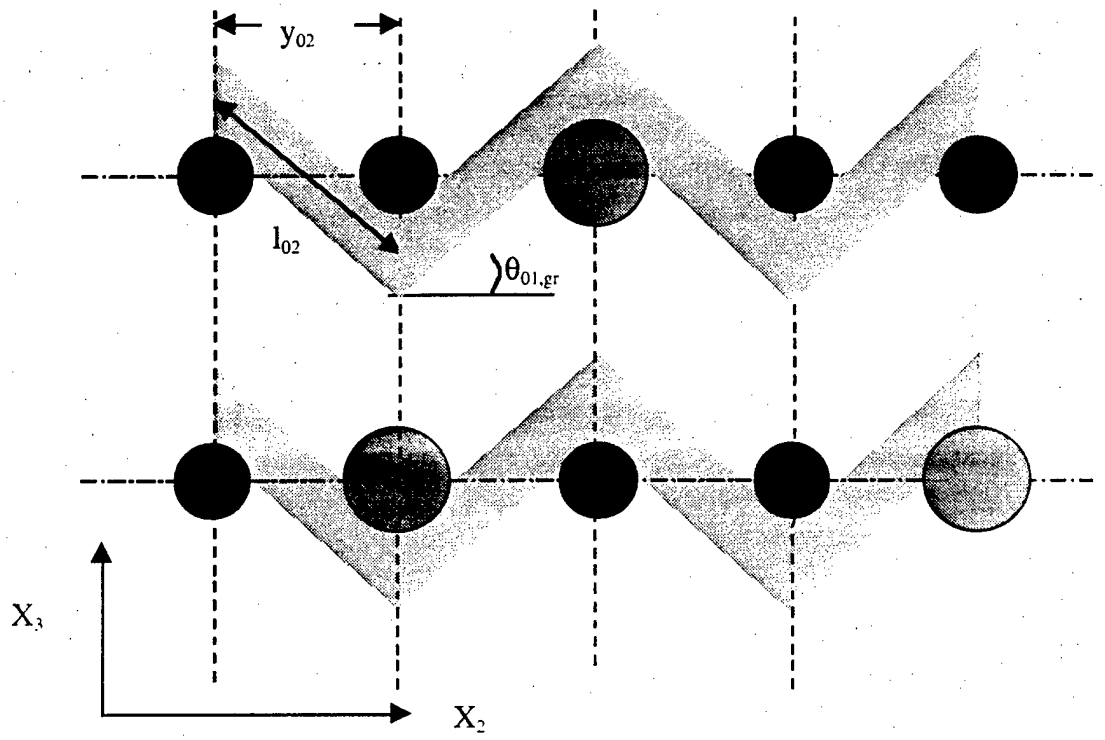

Figure 3.8 geometrical model: schematic view of the baseline structure in filling direction

3.6. The Tensile Characteristics of the Model

The tensile response of the 3-D fabric subjected to extension by an applied load along its length, warp direction, is estimated with the value of the sum of the single tensile forces acting on the ground weave, on the stuffers and on the binder yarns:

$$F_1 = n_{gr}F_{gr} + n_{bi}F_{bi} + n_{stf}F_{stf} \qquad (3.29)$$

where n_{gr} = total number of ground ends

n_{bi} = total number of binders

n_{stf} = total number of stuffers

F_{gr} = tensile force acting on a single ground end

F_{bi} = tensile force acting on a single binder end

F_{stf} = tensile force acting on a single stuffer end

For calculating the forces on each single ground or binder, the equation of the tensile force from Kawabata's uniaxial deformation theory is used, while the load-extension behavior of the stuffers is assumed to be the same as that of the threads used, thus in the above formula:

$$F_{gr} = g(\lambda_{y1})\sqrt{1-\left(\frac{2C_0 + C_1 l_{01}\cos\theta_{01}}{4g(\lambda_{y1}) + C_1 l_{01}\lambda_{y1}}\right)^2}$$

$$F_{bi} = g(\lambda_{y1})\sqrt{1-\left(\frac{2C_0 + C_1 l_{01}\cos\theta_{01}}{4g(\lambda_{y1}) + C_1 l_{01}\lambda_{y1}}\right)^2}$$

$$F_{stf} = g(\lambda_1)$$

Kawabata's uniaxial deformation theory is used also for calculating the stretch ratio on the fabric, thus using equation (3.12),

$$\lambda_1 = \frac{l_{01}\lambda_{y1}}{y_{01}}\sqrt{1-\left(\frac{2C_0 + C_1 l_{01}\cos\theta_{01}}{4g(\lambda_{y1}) + C_1 l_{01}\lambda_{y1}}\right)^2}$$

As explained in above, if the geometrical model considers zero crimp for the filling yarn, the calculations are simplified and the total force on the ground ends is given by the total number of ground ends multiplied the force acting on the single end as in equation (3.29). In this case, all the geometrical parameters needed to solve the equation of the tensile force are easily derived from the number of ends and picks per unit length and the diameters of the different yarns. If no assumptions are made on the

yarns crimp, the final total force on the grounds is an average of the total forces calculated using different geometrical model implying different angles at the interlacing points due to the presence of a binder thread adjacent to the ground end or to the presence of a float underneath.

For the calculation of the tensile response of the binder threads, similar considerations are made. The angles at the interlacing points are calculated using the proper formulas already given above for the binder threads. But double the number of picks per centimeter is considered in this case to get the average warp spacing, because the binders interlace with the fillings of both the top and the bottom layers of the 3-D fabric. Moreover, due to the sequence and mechanism of filling insertion, the filling yarns of the two layers are not aligned on the same vertical axis, and indeed the yarns of one layer are placed between the fillings of the other.

Other clarifications have to be made about Kawabata's equation used in our model for calculating the tensile force on a single ground or binder and about the equation giving the stretch ratio of the fabric.

The tensile properties of the ground or binder yarns are expressed in Kawabata's equations with a function of the yarn stretch ratio $g(\lambda_{y1})$ starting from a value of $\lambda_{y1}<1$ which corresponds to a stretch ratio λ_1 on the fabric equal to unity. This could appear impossible since by definition the stretch ratio must be a number greater than unity. The explanation was found in the fact that when the fabric (identified with the stuffers) starts to stretch, the ground and the binder yarns first straighten as much as possible and then stretch. Thus, at the beginning only the stuffers respond to the external loading with a tensile response given by $g(\lambda_1)$. The real response of the ground and binder ends starts after a while when $\lambda_{y1}=1$; before that point the negative force computed using Kawabata's equation is not really taken into account in the calculation of the total force acting on the 3-D fabric. Although the negative values of $g(\lambda_{y1})$ for $\lambda_{y1}<1$ have no physical meaning, they are in any case necessary for calculating the fabric stretch ratio λ_1 from its initial value equal to unity.

In the application of Kawabata's uniaxial deformation theory to the 3-D structure another modification was done, that is to consider the geometrical momentum of inertia of the filling fibers bending as referred to the central axis of the entire fabric in filling

direction. Thus, considering the parallel axis theorem, the geometrical momentum of inertia of a fiber is computed as:

$$I_f = I_{0f} + A_{ff}(\Delta s)^2 \qquad (3.30)$$

where I_{0f} = geometrical momentum about the principal axis of inertia of one external ground layer in the 3-D structure

A_{ff} = cross sectional area of a filling fiber

Δs = mean distance of a filling fiber from the principal axis of inertia of the 3-D structure

The final tensile model that was used for predicting the tensile response of the new developed structures, besides considering the geometrical model with zero filling yarn crimp, was further more modified and simplified because no tensile force was considered to act on the binders. The effect of the tensile force on the binders was in fact evaluated to be only the 0.1% of the total force on the 3-D fabric and thus it was neglected.

3.7. The System of Equations for the Model

The complete system of equations of the 3-D fabric model consists of some equations derived from the geometrical characteristics of the model and other equations that come from the mechanical characteristics of the model.

We report the system of equations that was used in the research for predicting the tensile force of the 3-D fabric with different type of fibers for grounds, binders, stuffers and filling yarns. The system of equations is derived from the geometrical model with zero filling yarn crimp, and from the tensile model with no binders contribution to the final tensile force of the fabric.

0.1.1. Geometrical equations

$$y_{01} = \frac{1}{ppc},\ y_{02} = \frac{1}{epc},\ \tan\theta_{01,gr} = \frac{y_{01}}{d_f + d_{gr}},\ \sin\theta_{02} = \frac{1}{S_1 + 1}$$

$$l_{01} = \frac{y_{01}}{\sin\theta_{01}},\ l_{02} = \frac{y_{02}}{\sin\theta_{02}},\ \lambda_1 = \frac{l_{01}\lambda_{y1}}{y_{01}}\sqrt{1 - \left(\frac{2C_0 + C_1 l_{01}\cos\theta_{01}}{4g(\lambda_{y1}) + C_1 l_{01}\lambda_{y1}}\right)^2}$$

$$A_{uc} = n_{stf}\,A_{stf},\ D_{stf} = \frac{A_{stf}}{w_{uc}},\ t = \max\left(D_{stf} + 2(d_f + d_{gr})\right)$$

$$\Delta s = \frac{t}{2} - d_w,\ I_{0f} = \frac{\pi d_f^{\,4}}{64},\ I_f = I_{0f} + A_f \Delta s^2$$

0.1.2. Mechanical Equations

$$C_b = 2N\frac{192 E_f I_f}{(2l_{02})^3},\ K = \frac{2\mu D}{l_{02}},$$

$$C_1 = \frac{C_b}{1 + 2K},\ C_0 = -\Phi_{max} C_1$$

$$F_{gr} = g(\lambda_{y1})\sqrt{1 - \left(\frac{2C_0 + C_1 l_{01}\cos\theta_{01}}{4g(\lambda_{y1}) + C_1 l_{01}\lambda_{y1}}\right)^2}$$

$$F_{stf} = g(\lambda_1)$$

$$F_1 = n_{gr}F_{gr} + n_{stf}F_{stf}$$

By knowing the fibers', yarns' and fabric's geometrical parameters and the yarns' mechanical parameters, it was possible to solve the above system of non-linear equations.

With the use of the computer was possible to insert other variables in the program to get the final tensile response of different parts of the fabric designed to have different types of fibers playing the role of grounds, binders or stuffer yarns. Thus, for example, using the variables k_A and k_B as the percentage of stuffers of fiber type A and the

percentage of stuffers of fiber B, the above formulas were modified as:

$$A_{uc} = n_{stf}(k_A A_{stfA} + k_B A_{stfB})$$

$$F_1 = n_{gr} F_{gr} + n_{stf}(k_A F_{stfA} + k_B F_{stfB})$$

and the model directly predict the tensile response of different parts of the fabric with different elastic modulus.

3.8. Application of 3D Woven Model

The woven fabric considered in the present paper is a tubular double–cloth structure consisting of two plain weave ground layers joint together by means of binder threads every two repeats. In each unit cell, delimited by the two plain weave layers and the binder threads, a certain number of stuffer yarns is inserted to reinforce the fabric in warp direction.

The 3-D weave is modeled with the purpose of creating a functionally graded structure, which has heterogeneous tensile characteristics down its length. The fabric is therefore considered as formed by two parts having the same weave but with different types of yarns, with different tensile characteristics, playing the role of grounds, binders or stuffers. (Fig.1). The design of the low modulus part of the fabric considers PEN grounds and binders, nylon 6 stuffers and polyester filling yarns. The design of the high modulus part is derived from the previous one making some or all the PEN grounds and binders change their role with a correspondent number of nylon 6 stuffers. In the manufacture of the fabric, this is achieved changing the pattern chain of the loom, with no need of adding or removing yarns, or of binding different types of stuffer yarns with different tensile properties by means of a splicer.

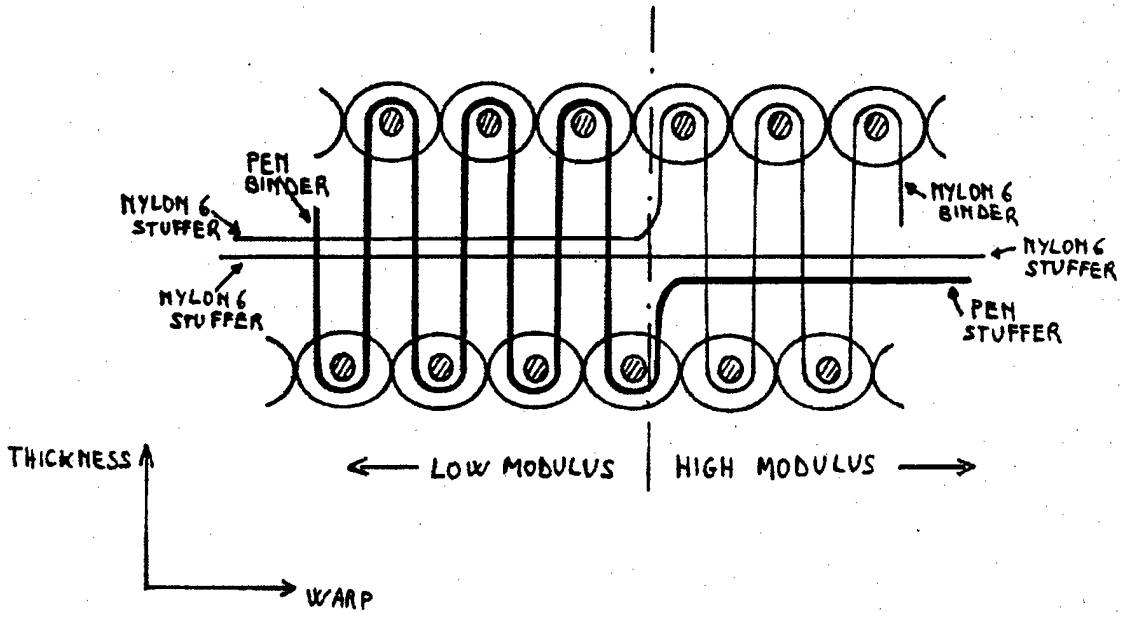

Figure 3.8 Schematic cross-section of the 3-D fabric in warp direction, showing the transition between the low modulus part and the high modulus part.

Tensile tests were conducted on prototypes of the novel structure (detailed in Table 3.1) in which the low modulus part had 100% nylon 6 stuffers while the high modulus part contained 95% nylon 6 and 5% PEN stuffers, and are summarized in Table 3.2.

Table 3.1. Fabric, Yarns and Fibers Parameters

Fabric Parameters			
Epc	10.75		
Ppc	3		
Unit cell width w_{uc} (cm)	0.4		
Filling yarn crimp S_2	0		
Fibers and Yarns Parameters			
Fiber	Nylon 6	PEN	Polyester
Yarn denier L_y	5040	7000	5040
filaments per yarn N	612	980	420
Fiber diameter (cm)	3.2×10^{-3}	2.7×10^{-3}	3.5×10^{-3}
Yarn diameter (cm)	0.103	0.108	0.093
Fiber area (cm^2)	8.17×10^{-6}	5.67×10^{-6}	9.66×10^{-6}
Yarn area (cm^2)	83.33×10^{-4}	92.6×10^{-4}	67.63×10^{-4}
Coefficient of friction μ	0.11	0.13	0.11
Max. decrease in thickness (cm) δ_{max}	0.0397	0.0336	0.0335
Fiber Young's modulus (kg/cm^2)	5.3×10^4	19.7×10^4	8.5×10^4

Table 3.2. Theoretical and experimental results

Sample	Theoretical Breaking Load (kg)	Experimental Breaking Load (kg)	Theoretical Thickness (cm)	Experimental Thickness (cm)
Baseline	62,260	69,605	0.910	0.870
Low Modulus	62,490	77,310	0.903	0.960
High Modulus	60,525	72,705	0.905	0.922

These data are graphically illustrated in Figures 3.9 and 3.10.

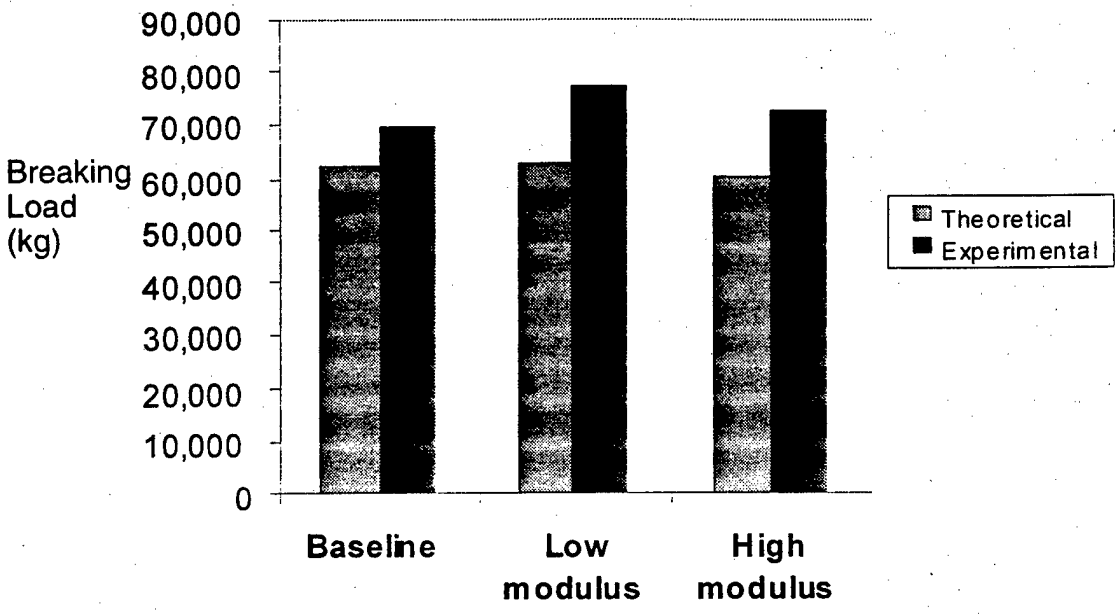

Figure 3.9 Comparison of Experimental and Theoretical Breaking Loads for three different 3D woven fabrics.

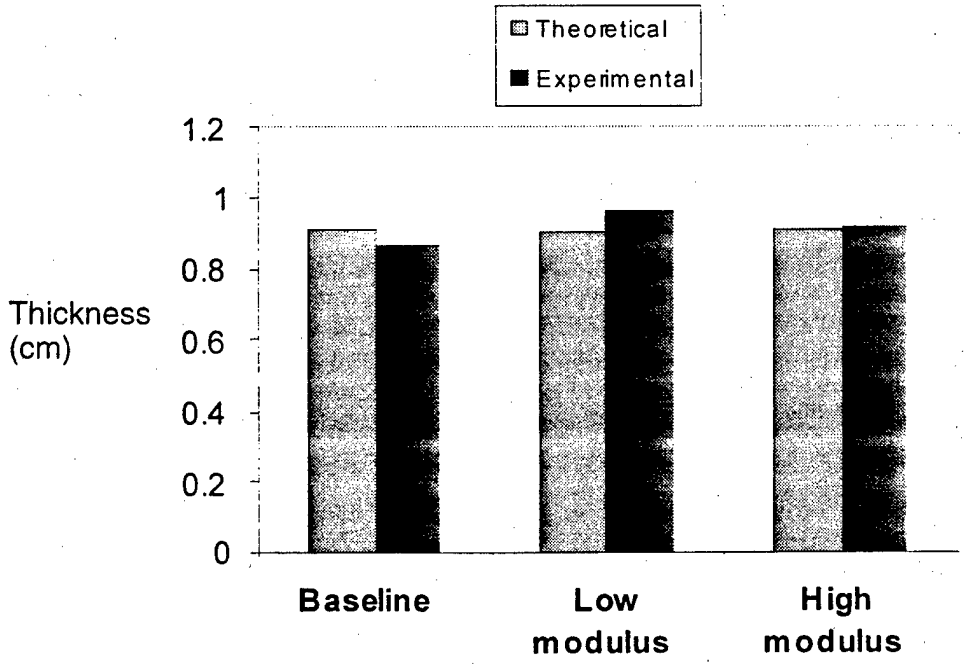

Figure 3.10 Comparison of Experimental and Theoretical Fabric Thicknesses for three different 3D woven fabrics.

Theoretical predictions of a family of fabrics with varying blend ratios of stuffer yarns is shown in Figure 3.11.

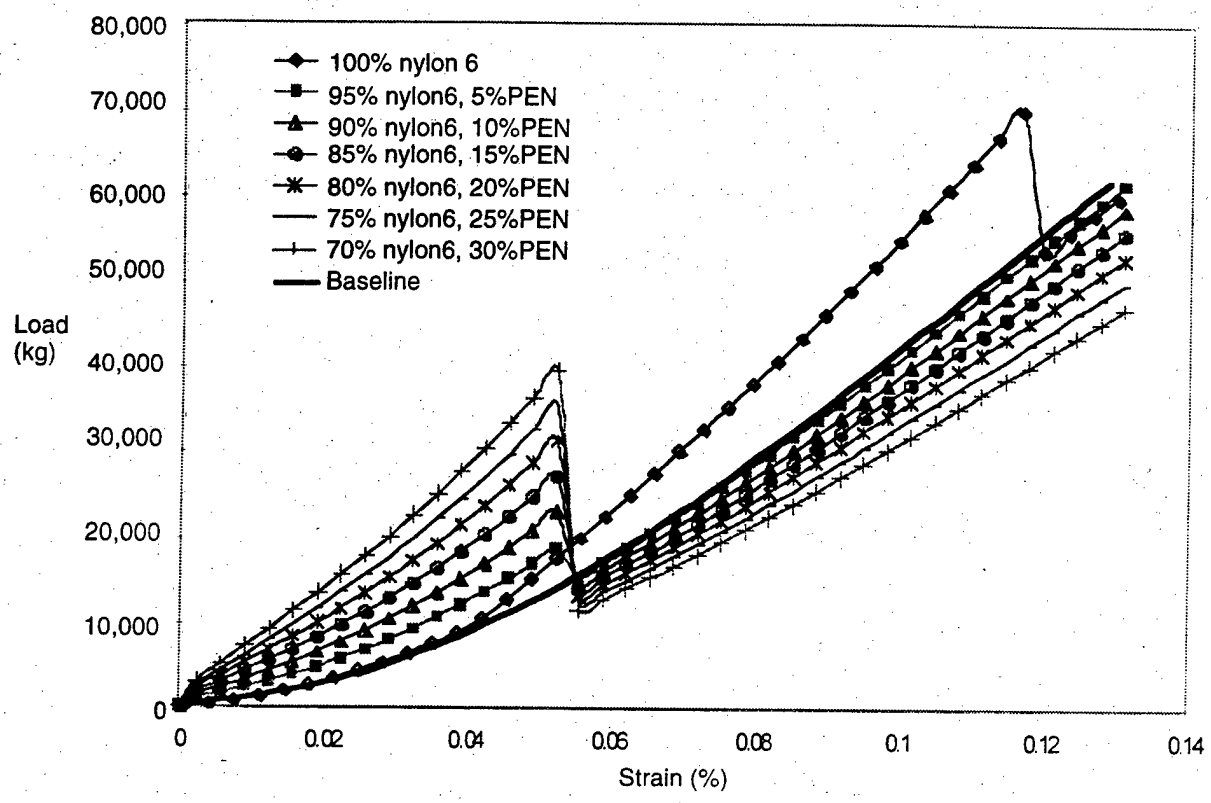

Figure 3.11 Comparison of theoretical predictions of 3D woven fabrics with different blend ratios for the stuffer (0°) yarns.

CONCLUSIONS

A novel 3-D impact contact variational analysis approach presented in this report enables to solve a variety of impact deformation and failure problems of composite structures having rectangular configurations. Composite structures characterized by a step-wise material property variation in one, two or three coordinate directions can be analyzed. The mathematical problem formulation takes full consideration of the 3-D transient nature of the deformation processes in a structure exposed to impact loading and, specifically, allows one to analytically study complex stress wave propagation in all three coordinate directions.

The adopted impact contact model assumes that only the mass, initial velocity and shape of the projectile are known. The contact pressure distribution is obtained directly from the solution. The developed analysis approach is capable of solving both thin and thick structural elements made from conventional laminates, from 3D textile reinforced composites, and hybrids of thereof.

Considered numerical examples verify accuracy of the developed computational algorithm and computer code. A number of characteristic 3-D impact effects are revealed and interpreted. A comparison presented for 3D woven and traditional laminated composite plates provides a useful information for designing impact-resistant composite structures.

An extension of Kawabata's uniaxial deformation theory for plain weaves have been proposed for predicting the tensile response of a novel 3-D woven structure.

A good agreement was found between the theoretical and the experimental results for both the final breaking load values and the thickness values of the manufactured prototypes of the 3-D novel fabric.

4. REFERENCES

1. C. M. Pastore and A. E. Bogdanovich, "A Comparative Theoretical Study of Quasi-Static and Impact Response of Laminated and Textile Composite Structures", *Interim Technical Report, ARO Grant DAAH04-96-1-0057*, December, 1997.
2. C. M. Pastore and A. E. Bogdanovich, "A Comparative Theoretical Study of Quasi-Static and Impact Response of Laminated and Textile Composite Structures", *Interim Technical Report, ARO Grant DAAH04-96-1-0057*, December 1998.
3. Pagano, N. J., "Exact solutions for composite laminates in cylindrical bending, *J. Compos. Mater.*", 1969, Vol. 3, pp. 398-411.
4. C. M. Pastore and A. E. Bogdanovich, "A Comparative Theoretical Study of Quasi-Static and Impact Response of Laminated and Textile Composite Structures", *Interim Technical Report, ARO Grant DAAH04-96-1-0057*, December, 1996.
5. Mohamed, M.H. and Zhang, Z.H., "Method of Forming Variable Cross-Sectional Shaped Three-Dimensional Fabrics", *U.S. Patent No. 5085252*, 1992.
6. Anandjiwala, R.D., and Leaf, G.A.V., "Large-Scale Extension and Recovery of Plain Woven Fabrics", *Textile Res. J.* **61** (11), 619-634 (1991).
7. Anandjiwala, R.D., and Leaf, G.A.V., "Large-Scale Extension and Recovery of Plain Woven Fabrics, PartII: Experimental and Discussion", *Textile Res. J.* **61** (12), 743-755 (1991).
8. Della Putta, L., "Design of a Novel 3-D Woven Fabric", Master Thesis, PCT&S, Philadelphia, (1998).
9. Grosberg, P., and Kedia, S., "The Mechanical Properties of Woven Fabrics, PartI: The Initial Load Extension Modulus of Woven Fabrics", *Textile Res. J.* **36**, 71-79 (1966).
10. Hearle, J.W.S., Grosberg, P., and Backer, S., "Structural Mechanics of Fibers, Yarns, and Fabrics", Wiley & Sons, New York, 1969.
11. Kawabata, S., Niwa, M., and Kawai, H., "The Finite-Deformation Theory of Plain-Weave Fabrics, Part I: The Biaxial-Deformation Theory", *J. Textile Inst.* **64** (2), 21-46 (1973).
12. Kawabata, S., Niwa, M., and Kawai, H., "The Finite-Deformation Theory of Plain-

Weave Fabrics, Part II: The Uniaxial-Deformation Theory", *J. Textile Inst.* **64** (2), 47-61 (1973).

13. Kawabata, S., Niwa, M., "A Finite-Deformation Theory of the 2/2-Twill Weave Under Biaxial Extension", *J. textile Inst.* **70** (10), 417-426 (1979).

14. Kemp, A.J., "An Extension of Peirce's Cloth Geometry to the Treatment of Non-circular Threads", *J. Textile Inst.* **49**,T44-T51 (1958).

15. Kilby, W.F., "Planar Stress-strain Relationships in Woven Fabrics", *J. Textile Inst.* **54**, T9-T27 (1963).

16. Olofsson, B., "A general Model of a Fabric as a Geometric-Mechanical Structure"" *J. Textile Inst.* **55**, T541-T557 (1964).

17. Peirce, F.T., "Geometry of Cloth Structure", *J. Textile Inst.* **28**, T45-T96 (1937).

18. Realff, M.L., Boyce, M.C., and Backer, S., "Micromechanical Approach to Modelling Tensile Behaviour of Woven Fabrics", in "Proc.1993 ASME Winter Annual Meeting", MD-vol. 46, Use of Plastics and plastic Composites: Materials and Mechanics Issues, ASME, 1993, pp.285-294.

19. Realff, M.L., Boyce, M.C., and Backer, S., "A Micromechanical Model of the Tensile Behaviour of Woven Fabric", *Textile Res. J.* **67** (6), 445-459 (1997).

20. Reumann, R.D., CAD Method for the Predetermination of the Weave-Related Load-Extension Characteristics of Woven Fabrics", *Melliand Textilber.* **11**, E386-E388 (1990).

21. Shanahan, W.J., and Hearle, J. W.S., "An Energy Method for Calculations in Fabric Mechanics, Part I:Principles of the Method", *J. Textile. Inst.* **69**, 81-91 (1978).

22. Shanahan, W.J. and Hearle, J.W.S., "An Energy Method for Calculations in Fabric Mechanics, Part II: Examples of Application of the Method to Woven Fabrics", *J. Textile Inst.* **69**, 92-100 (1978).

23. Sharkas, M.Y., Leaf, G.A.V., "The Initial Load-Extension Properties of 2/2 Twill Woven Fabrics", Ph.D. Thesis, Dept. of Text. Ind., The University of Leeds, England, Oct.1987.

24. Sun, F., Seyam, A.M., and Gupta, B.S., "A Generalized Model for Predicting Load-Extension Properties of Woven Fabrics", *Textile Res. J.* **67** (12), 866-874 (1997).